ADVANCED FUNCTIONAL MATERIALS
www.afm-journal.de

Strategies for Realizing Rechargeable High Volumetric Energy Density Conversion-Based Aluminum–Sulfur Batteries

Jing Zhang, Rong He, Lujie Jia, Caiyin You, Yongzheng Zhang, Meinan Liu, Na Tian, Hongzhen Lin,* and Jian Wang**

Aluminum–sulfur batteries (ASBs) are deemed to be alternatives to meet the increasing demands for energy storage due to their high theoretical capacity, high safety, low cost, and the rich abundances of Al and S. However, the challenging problems including sluggish conversion kinetics, inferior electrolyte compatibility, and potential dendrite formation are still remained. This review comprehensively focuses on summarizing the specific strategies from polysulfide shuttling inhibition to form smooth anodic Al activation/deposition. Especially, innovations in cathodic side for achieving electrochemical kinetic modulations, electrolyte optimizations, and anodic interface mediations are discussed. Upon detailed elaborating the formation process, influencing factors, and their interactions in the Al–S electrochemistry, a comprehensive summary of their causative mechanisms and the corresponding strategies are provided, including optimization of electrolytes, innovative in situ detections, and precise electrocatalytic strategies. Based on such a systematic understanding in the Al–S electrochemistry, the possible electrochemical reaction mechanism is deciphered more clearly and enlightened practical strategies on the future development of stable ASBs. Furthermore, future opportunities and directions of high-performance conversion-based Al–S batteries for large-scale energy storage applications are highlighted.

1. Introduction

Advanced rechargeable batteries have become viable options nowadays to meet the ever-increasing demand for energy storage and conversion devices.[1] And they have performed a profound impact on alleviating environmental pollution, providing solutions to ever-increasing energy crisis, and shifting energy consumption patterns from traditional fossil fuels to renewable energy.[1e,2] Among the state-of-art batteries, rechargeable lithium metal batteries (LMBs) are increasingly attractive owing to their high theoretical storage capacity of 3860 mA h g^{-1}.[3] Unfortunately, the wide application of LMBs will be limited by the resources, high cost, safety concerns of dendrite formation, as well as their relatively low volumetric energy density.[4] Accordingly, new battery systems with low cost and high security are intensively desired for the future widespread practical applications.[5]

Recently, rechargeable aluminum batteries are considered as the potential alternatives due to their low cost, high chemical stability than metal Li, nearly 3 times of volumetric storage capacity greater than that of Li metal (8046 vs 2980 mA h cm^{-3}) and the most abundant metal reservation of Al in the earth's crust,[6] as presented in **Figure 1**A. More importantly, Al metal is less sensitive to moisture, making cell fabrication much easier and more convenient in aqueous or nonaqueous electrochemical storage systems.[5a–c,7] Up to date, diverse cathode materials have been attempted to couple with the Al anode, usually divided into two categories according to their

J. Zhang, R. He, C. You, N. Tian
School of Materials Science and Engineering
Xi'an University of Technology
Xi'an, Shaanxi 710048, China
E-mail: caiyinyou@xaut.edu.cn

The ORCID identification number(s) for the author(s) of this article can be found under https://doi.org/10.1002/adfm.202305674

DOI: 10.1002/adfm.202305674

L. Jia, M. Liu, H. Lin, J. Wang
i-Lab & CAS Key Laboratory of Nanophotonic Materials and Devices
Suzhou Institute of Nano-Tech and Nano-Bionics
Chinese Academy of Sciences
Suzhou 215123, China
E-mail: hzlin2010@sinano.ac.cn; jian.wang@kit.edu

Y. Zhang
State Key Laboratory of Chemical Engineering
East China University of Science and Technology
Shanghai 200237, China

J. Wang
Helmholtz Institute Ulm (HIU)
D89081 Ulm, Germany

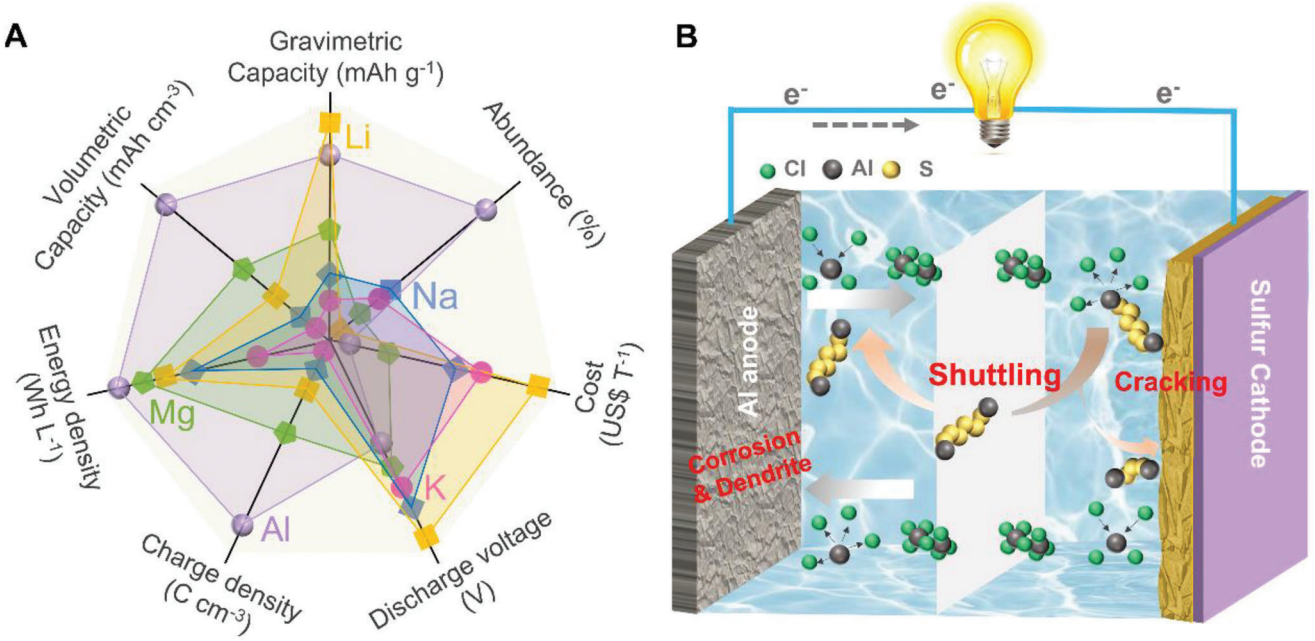

Figure 1. A) Schematic comparison of the Al, Mg, Li, K and Na based anode in energy storage systems from seven key indicators.B) Charge/discharge evolution of an Al–S battery in $AlCl_3$ related ionic liquid electrolyte.

electrochemical reaction mechanisms, i.e., the conversion-based sulfur or oxygen cathodes,[6e,8] and intercalation/deintercalation-based carbon materials,[9] metal oxides and metal sulfides.[2e,6g,10] Among them, elemental sulfur has the theoretical specific capacity (1675 mA h g^{-1}), low cost and environmental friendliness than the other cathodes.[6a,c,11] The rechargeable aluminum–sulfur batteries (ASBs) are believed to be the most potential candidate among the aluminum batteries to output high volume energy density.[12]

Similar to the lithium–sulfur (Li–S) batteries, the Al–S batteries are composed of aluminum foil as anode and the elemental sulfur supported by conductive matrices as cathode in an organic/aqueous electrolyte.[6a,b,8d,12b,13] During charging/discharging process, metallic Al anode usually tends to form a dense passivation layer of Al_2O_3 to increase its inertness at the electrolyte/electrode interface.[14] Meanwhile, the mobility of Al ions in the electrolyte becomes much sluggish owing to the high valence and space hindrance. Therefore, the electrolyte properties can greatly affect the conversion and diffusion kinetics in Al–S batteries. At the beginning, the electrochemically reversible feasibility of aluminum was uncovered in a temperature-dependent chloroaluminate bath.[15] Inspected by this, various aqueous electrolytes have also been attempted as alternatives to pursue a more feasible and stable electrochemical reaction of S with Al.[6c,11b,13d,16] Meanwhile, room temperature ionic liquids (RTIL) such as chloroaluminate and imidazolium salts along with aluminum chloride were designed and adopted into Al–S batteries to improve the stripping/plating kinetics towards high coulombic efficiency.[8d,13b,17] With the aid of the nonaqueous or aqueous-based electrolyte, it is possible to realize the reversibility of rechargeable Al–S batteries. Up to now, the detailed electrochemical reaction mechanisms of Al–S batteries remain uncertain and even unknown. Taking $AlCl_3^-$based ionic liquid electrolyte as an example, the electrochemistry of the Al–S batteries possibly undergoes the following reactions during the redox process:[6b,8d,13d]

$$2Al + 14AlCl_4^- \rightarrow 8Al_2Cl_7^- + 6e^- \quad (1)$$

$$4Al_2Cl_7^- \rightarrow 7AlCl_4^- + Al^{3+} \quad (2)$$

$$2Al^{3+} + 6e^- + 3S \rightarrow Al_2S_3 \quad (3)$$

It is obvious that the common electrolytes usually do not contain high concentrations of free Al^{3+} ions, while the $AlCl_4^-$ ion in the electrolyte works as the intercalated mediator and reacts with Al metal to generate more $Al_2Cl_7^-$ species. The formed $Al_2Cl_7^-$ ions then move across the separator to reach the sulfur electrode and dissociated to further release Al^{3+} ions under the electronic field, as described in Equation (2). Such free Al^{3+} ions at the sulfur side directly react with sulfur to dominantly generate Al_2S_3 through 6-electron transference reactions. Overall, Equations (2) and (3) contain the multistep electrochemical reactions in the discharge process, slowing down the reaction kinetics with high barriers.[8d]

Apart from the dominantly insulative product of Al_2S_3, similar to Li–S batteries, it is inevitable to generate the soluble polysulfide intermediates such as Al_2S_6, Al_2S_{12}, and Al_2S_{18} in the liquid electrolyte due to the multistep conversions, resulting in the so-called "shuttle effect" (Figure 1B).[18] From the above electrochemical reaction steps, it is not hard to find that the development of an effective rechargeable Al–S battery is significantly hindered by the slow transfer kinetics and reversibility of the charge–discharge process, which are the key challenges remained to be addressed urgently. On the one hand, the viscosity and carrier size of the state-of-the-art room-temperature

electrolyte for Al–S batteries are several tens of times larger than the Li ions in ether-based electrolyte used in Li–S batteries, causing the much-depressed ionic conductivity in the electrolyte.[19] Such poor mobility and conductivity of electrolyte together with the insulative sulfur and Al_2S_3 would suffer from more obstacles of the ion/electron transport, bringing about sluggish reaction kinetics in Al–S batteries.[20] On the other hand, the shuttle effect of the accumulated polysulfides resulted from the sluggish electrochemical kinetics would reduce the utilization ratio of the sulfur and Al, worsening the reversibility.[21] Lastly, the uneven plating/stripping aluminum behaviors on the Al anode and the migrated polysulfides react with metallic aluminum can induce the formation of a thin passivation layer, leading to sluggish aluminum diffusion kinetics and depressive cycling lifespan.[22]

Although diverse efforts have been made to address the above-mentioned drawbacks in the rechargeable Al–S batteries, the resolution strategies of the up-to-date researches are still at the early stage and insufficient to adapt their practical applications. In the past few years, most investigations were focused on designing or developing suitable host materials or optimizing the compatible electrolytes to quest for high-performance Al–S systems.[6a,c,11b,c,12a–c,16a,23] The detail methods can be categorized into following aspects: i) designing high conductive matrix to support the insulative sulfur for fast charge transfer during electrochemical reactions;[7a,12c,h,13d,24] ii) developing heteroatoms doped and porous structure to physically/chemically anchor diffluent S-containing species for high reversibility performance;[8b,g,25] iii) introducing appropriate composition proportion to explore new electrolyte systems to couple with sulfur cathode and Al anode for high reaction kinetics and low potential polarization.[6a,b,8d,13b,d] However, there is still lack of systematic landscapes for further developments on Al–S batteries. Therefore, a comprehensive review from diverse aspects including cathode materials, electrolytes, and Al anode protection to summarize the advanced strategies for high-performance Al–S batteries is becoming more necessary at this early research stage.

In this review, we will comprehensively summarize recent studies concentrated on the specific strategies to inhibit polysulfides shuttling and to form smooth Al anode for triggering the development of Al–S batteries with aspects of sulfur cathode, Al anode as well as electrolyte optimization compatibility (**Figure 2**). Specifically, innovations in cathode structures for achieving electrochemical kinetics modulation, electrolyte matching, and anodic interface mediation are disseminated. Based on the progress made with the combination of theoretical simulations and electrochemical characterizations, we will further present the possible electrochemical reaction mechanism of Al–S batteries more clearly. Furthermore, the challenges and prospects of high-performance conversion-based Al–S batteries, and the future directions for further improvements are enlightened.

2. Adsorption-Catalysis Strategies toward High-Efficiency Sulfur Conversion and Preservation

Elemental sulfur, as a characteristic conversion-type cathode,[22c,26] matching with aluminum anode deserves to be attractive from construction designs to mechanism understandings due to its low cost and high theoretical capacity.[24a,b]

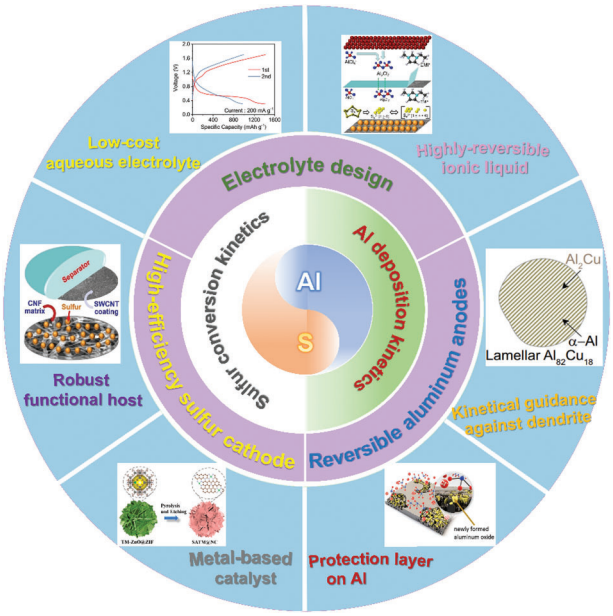

Figure 2. Summary of the recent studies concentrated on the specific strategies to inhibit polysulfide shuttling and to form smooth Al anode for triggering the sustainable development of Al–S batteries.

So far, several efforts have been made in Al–S batteries and the significantly improved capacities have been exhibited. However, several key challenges, i.e., insulative nature of S/Al_2S_3, polysulfide shuttling, and sluggish conversion kinetics still prevent the developments toward high performance.[7a,12h] With the ever-increasing requirements on high energy density, high sulfur loading cathodes are necessary for achieving high areal capacities and volume energy densities, which would cause more severe problems.[27] In this section, the host design with the polar sites introduction is used to strengthen polysulfides adsorption. In view of the saturated trapping sites for high sulfur-loading cathodes, the common adsorption strategies still face a worrisome shuttling phenomenon, which would cause cell failures in the long-term working. To fully resolve the above issues, the combined "adsorption-catalysis" strategies are proposed to take full use of the independent advantages together to relieve the accumulation of sulfur species through boosting conversion kinetics.[20a] In the latter, the metal-based catalysts are briefly introduced to effectively propel the interconversion kinetics for high sulfur utilization and low battery polarization.

2.1. Conventional Conductive Carbon Hosts for Embedding Sulfur

Carbon materials have the superiority in conductivity and could enhance the entire conductivity of sulfur/carbon composites, simultaneously serving as a porous conductive infrastructure to accommodate the sulfur species. Encapsulating sulfur in conductive carbonaceous materials, such as graphene,[24c] carbon nanotubes/nanofibers,[13d] and nanocarbon derived from metal organic frameworks (MOFs) etc.,[12c] become one of the most promising approaches to improve the practical capacity and cycle stability. For example, Manthiram's group demonstrated a

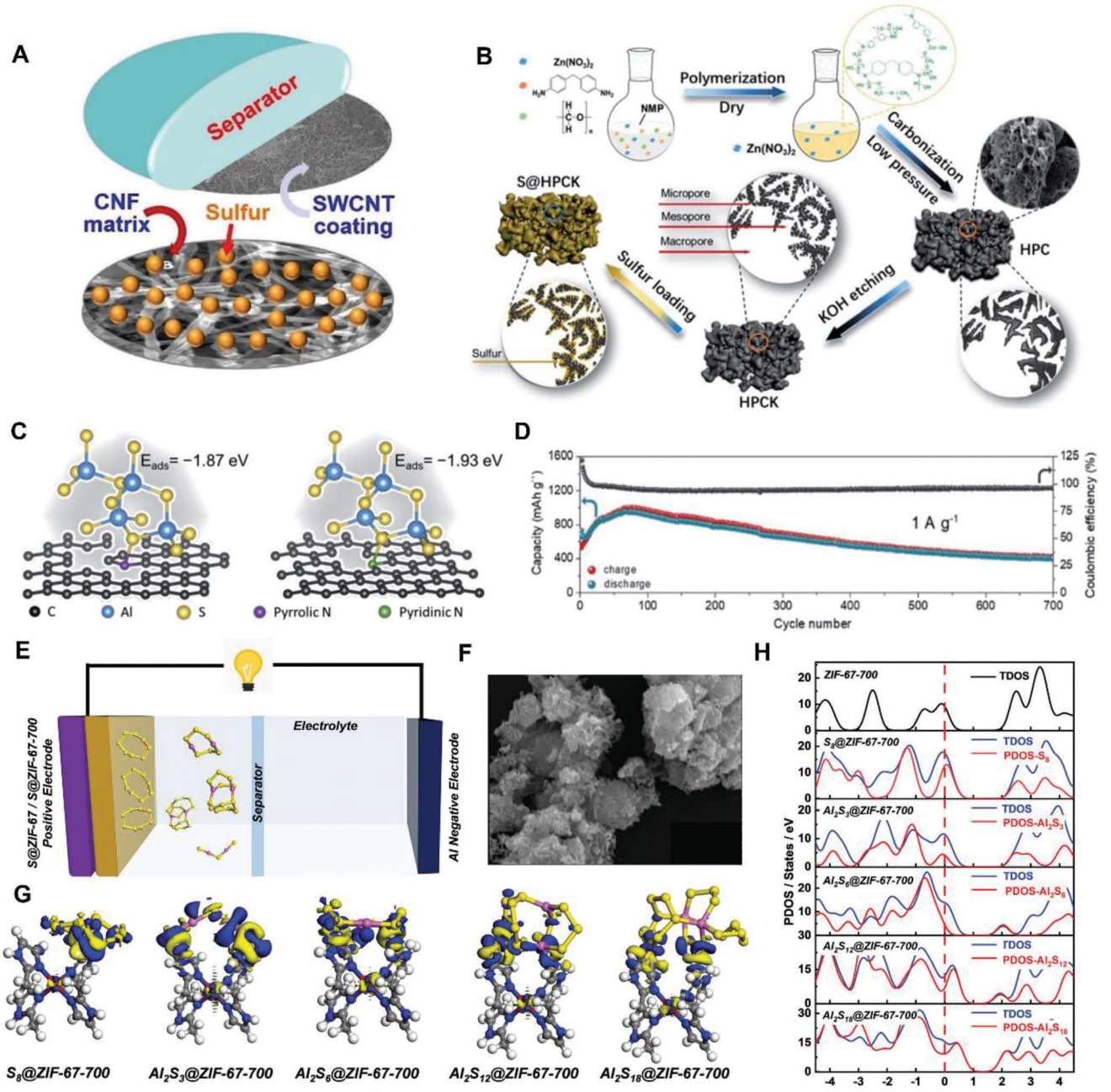

Figure 3. A) Schematic description of an CNF supported electrode with SWCNT coated separator assembly for a nonaqueous room-temperature Al–S battery. Reproduced with permission.[13d] Copyright 2017, Wiley-VCH GmbH. B) Schematic illustration of the preparation of HPCK and S@HPCK. C) Representative models and adsorbed energies of pyrrolic N and pyridinic N interacted with tetra-coordinated Al_2S_3. D) Long lifespan cycle performance at a current density of 1 A g^{-1}. Reproduced with permission.[8g] Copyright 2021, Royal Society of Chemistry. E) Schematic illustration of the proposed Al–S batteries using MOFs and MOF-derived material as host materials; F) SEM image of S@ZIF-67-700 composites. G) Charge density differences of ZIF-67-700 interacted sulfur species, respectively. H) Total density of states (TDOS) and partial density of states (PDOS) of ZIF-67-700, S_8@ZIF-67-700, and Al_xS_y@ZIF-67-700, respectively. Reproduced with permission.[25] Copyright 2021, Royal Society of Chemistry.

reversible room-temperature Al–S battery with a strategically designed cathode structure of spreading active sulfur into the ionic liquid and uniformly dispersed into a free-standing carbon nanofiber (CNF) paper matrix (**Figure 3**A).[13d] With the blocking effect of cross-linked single-wall carbon nanotube (SWCNT) coated on separator, the diffusion kinetics of polysulfide species to aluminum side is prevented and the electrochemical polarization is reduced. Although a high initial capacity (>1200 mA h g^{-1}) is released at 0.05 C, the discharge capacity of the as-prepared cell fades down to less than 600 mA h g^{-1} after 10 cycles due to the low

efficiency of polysulfides confinement constructed on the poor links between the sulfur and the carbon matrix. By the way, considering the additional mass weight of the SWCNT in the cathode side, the entire sulfur weight ratio in the electrode is rather low, so new methodology should be developed to confine polysulfide species more efficiently.

It seems quite effective to confine the soluble polysulfides in the cathodic side without migrating to the anodic side, which can significantly enhance the utilization efficiency. As an alternative way, coating or filtering porous materials on the separator seems an optimized way to construct a physical shield. Wei et al. used reduced graphene oxide coated separator as the polysulfide physical preventer layer in the room-temperature Al–S battery, acting as a sandwich-like architecture.[24b] With the aid of X-ray diffraction (XRD), X-ray photoelectronic spectroscopy (XPS), Raman and electronic microscopy, the transformation between sulfur and Al_2S_3 is much more reversible during the charge–discharge process. The cathode with a relatively high weight content of 48% displays a slightly increased cycling life of 38 cycles with the capacity fluctuation ranging from 1145 to 676 mA h g^{-1} at the current density of 50 mA g^{-1}.

For deep and detail understanding of the aluminum sulfur batteries, the ab initio molecular dynamics simulations were carried out to investigate Al_2S_3/electrolyte or S/electrolyte interface[12c] The formation of cationic/anionic intermediate species are revealed during the sulfur reduction process. Two main voltage domains exist in the initial reduction process: the former one (1.87–2.1 V) is the interface effect of surface/electrolyte to form the cathode/electrolyte interphase; and the latter one (1.38–1.50 V) is the multi-step transformation of sulfur to soluble high-order polysulfides and to Al_2S_3. However, in the charging process, the nonconductive Al_2S_3 discharged products experience three voltage domains and peaks, implying a gradual oxidation process. The Al_2S_3/electrolyte interface shows the structural distortion of the top atomic sublayer owing to the sluggish Al ion diffusion.

2.2. Polar Heteroatom Doping Strategies for Adsorbing Sulfur-Related Species

As widely acknowledged, heteroatom doping in the nanocarbon is capable of influencing the electronic density distribution of the intrinsic nanocarbon, leading to more active sites and functional groups simultaneously to enhance the chemical adsorption capability.[8b,22b] Recently, heteroatoms such as oxygen-, sulfur- and nitrogen-doped nanocarbons have been developed as modulators for chemical adsorption environments through hydrothermal reaction or polymer pyrolysis.[20b,21b] A N-doped hierarchical porous carbon (HPCK) was synthesized via a soft-template method,[8g] as illustrated in Figure 3B. The $Zn(NO_3)_2$ precursors sever as the pore formation reagent at high temperature by evaporating Zn. After KOH etching, effective electrolyte transport channels with hierarchical pore are obtained in the so-fabricated porous carbon, and it also provided the voids to accommodate active sulfur. The N-doped sites resulted from the carbonization of organics boost charge transfer and anchors aluminum polysulfide species. With the aid of theoretical simulation and density of states (DOS) calculation, the bandgap of S_8 is not changed or vanished and kept about 2.5 eV when touched with the pristine carbon. In contrast, an enhanced DOS curve is achieved at the Fermi level when introducing the nitrogen atom into the nanocarbon, suggesting the improved electrical conductivity with nitrogen dopants. Moreover, the nuclear magnetic resonance (NMR) analysis of the cycled sulfur cathode demonstrates the dominate discharge production is the formation of Al_2S_3 with the tetra-coordination configuration. Further, the binding energies (E_{ads}) of tetra-coordinated Al_2S_3 on the pyrrolic N and pyridinic N sites are calculated to be −1.87 eV and −1.93 eV (Figure 3C), respectively. That means the pyrrolic and pyridinic N centers in the HPCK have the capability to trap the polysulfides and modulate the deposition of the discharge product. Therefore, the as-prepared cathode employed with a low-cost $AlCl_3$/acetamide electrolyte delivers an excellent cyclability above 405 mA h g^{-1} at a current density of 1 A g^{-1} after 700 cycles (Figure 3D), bringing about the strengthened reversibility and utilization.

Apart from heteroatom doping carbon, sulfur cathode dispersed onto the other polar host materials such as metal-organic frameworks (MOFs) and MXene to reach improved electrochemical performance are also prosperous.[8c,25,28] Metal-organic frameworks (MOFs) are deemed as pop stars since they possess the merit of controllable configuration/ligand with adjustable porosity and chemical metal cores. Acting as the sulfur matrix, the MOFs or derivates are promising for realizing high-performance Al-S batteries via chemically adsorptions. For example, Jiao et al. employed ZIF-67 and ZIF-67-derived material pyrolyzed under 700 °C as sulfur hosts, respectively (Figure 3E).[25] Both the pristine ZIF and carbonized one reserve the well-defined porous morphologies (Figure 3F). As simulated in Figure 3G, charge density difference analysis was used to directly witness the active material/supporter interaction. It is found that apparent electronic charge accumulation and depletion are formed at the interfacial contact edge between the matrix and sulfur species and then extended to metal cores, proving that the core metal atom exhibits strong chemical adsorption toward the S or aluminum polysulfides. Furthermore, the total DOS and partial density of states are compared and strong electronic contributions from the substrates are monitored near the Femi level, indicating the improved electronic conductivity (Figure 3H). Thanks to these merits, the voltage hysteresis is significantly decreased down to ≈0.8 V after 50 cycles. At a current density of 300 mA g^{-1}, the as-prepared sulfur cathode remains the two-working charge/discharge voltage plateaus at 1.5 and 0.7 V, respectively, and delivers the capacity of 160 mA h g^{-1}.

The typical 2D transition metal carbides of MXene family possess inherent metallic conductive nature, tunable surface chemistry, and defect-rich sites, which make it potentially used in Al–S batteries. Wei's group designed a novel binder-free sandwich MXene layer, affording a conductive matrix with uniform sulfur dispersion ($S@Ti_3C_2T_x$) as the cathode.[28] The $Ti_3C_2T_x$ not only fictionizes as the binder and conductive agent but also acts as a promising host for sulfur species anchoring. As a result, $S@Ti_3C_2T_x$ flexible electrode displays an initial capacity of 489 mA h g^{-1} at 300 mA g^{-1} and still retains at 415 mA h g^{-1} after 280 cycles with an average Coulombic efficiency over 95%, which reveals the partially reversible redox reaction between Al_2S_3 and S. This attempt rises a facile and controllable electrode design for the development of Al–S batteries.

2.3. Metal-Based Hybrid Composites for Catalyzing Sulfur

Upon the simple adsorption strategy for inhibiting the shuttle effects of aluminum polysulfides, introducing the limited adsorption site numbers on the conductive matrices would become failed under the conditions of the continuous dissolution of formed polysulfides at high mass loading, resulting in degrading electrochemical performances.[29] Due to the deficient ability of hosts with adsorption only in the kinetical regulation,[11c] another "adsorption-catalysis" synergistic strategy is proposed, similar to Li–S batteries,[7c,14d] which is expected to fully resolve the above issues by lowering the accumulation of sulfur species through boosting the phase conversion kinetics.[30] Specifically, the high energy barriers of sulfur conversions are related to the slow diffusion kinetics in the insulative Al_2S_3 and polysulfide interconversions along with the ions in the electrolyte, bringing about poor sulfur reversibility and large voltage hysteresis.[8e]

At the beginning, the addition of transit metal nanoparticles attracted wide attention owing to their high conductivity and feasibility. To strengthen the adsorption chemistry, metal nanoparticles are usually hybridized with the carbon matrices. For example, incorporating Cu nanoparticles derived from a carbonized-MOF (HKUST-1-C) into sulfur host is deemed to enhance the conductivity of the porous matrix, acting as the active center as well (**Figure 4**A).[31] With the aid of spectroscopic analysis, the vital mechanistic insights of Cu on the electrochemical procedures were revealed via UV–vis absorption, Auger spectroscopy and XRD analysis of the fabricated cathode before and after cycling. In UV–vis spectroscopic measurements, the residual S_6^{2-} species remained on the separators are observed due to the solubility of S_6^{2-} in the ionic liquids. While the absence of low-chain S_x^{2-} is ascribed to the insoluble nature in the ionic liquids (ILs) electrolyte (Figure 4B). However, in the Auger spectrum of Cu LMM, the pristine cathode shows a peak located at 917.9 eV while it shifted down to 916.2 eV both in the charged and discharged states (Figure 4C), which may be interpreted by the strong interactions between Cu nanoparticles and polysulfides. Further, the XRD pattern measurements of the sulfur cathode were carried out at the various states. The feature peaks of Cu_xS come out during the whole process. Such strong interaction with the formation of Cu–S bond and the high electrical conductivity of Cu largely contribute to decrease of the kinetic barriers during electrochemical conversions, thereby increasing both S reversibility and specific capacity of the S@HKUST-1-C cathode.

In spite of Cu nanoparticle, the other 3d-orbit transition metal nanoparticles were also adopted. For instance, Ji's group successively demonstrated a Co-based electrochemical catalyst that rendered a reduced discharge–charge voltage hysteresis, improved capacity retention and rate capability for Al–S batteries.[31] The XPS analyses on the Co 2p and S 2p spectra suggest that the electrochemical catalytic reactions of sulfides in the cathode involve the valence state changes of cobalt between Co(II) and Co(III), which is closely associated with the formation of cobalt sulfides for propelling the catalytic interaction with the sulfur species. On the other hand, the current density of the symmetric cells cyclic voltammetry (CV) profiles in Figure 4D with Co(II) and Co(III) display the maximum current density value, demonstrating that the Co can enhance the reaction rate. On the heel of the CV measurement, a considerable reduction of the voltage hysteresis (0.8 V) is observed in the voltage profiles of the three cells (Figure 4E) in the presence of containing 1.0 wt% anhydrous $CoCl_2$ precursor. With the improved reaction activity expedited by catalytic Co(II) and Co(III) in the sulfur cathode, the utilization of sulfur is boosted to about 90%, signifying an improved reaction kinetics of the electrochemical conversion of sulfur in the Al–S batteries. Consequently, using an ionic liquid [EMIM]3.1Cl: $AlCl_3$ (mole ratio of 1:1.3) as the electrolyte, the catalytic cathode with Co active site delivers a high-rate capacity of ≈300 mA h g^{-1} at 3 A g^{-1} and still remains a reversible specific capacity of ≈500 mA h g^{-1} at 1 A g^{-1} after 200 cycles. Then, XRD patterns at the charged and discharged states in Figure 4F were acquired on the S@Co/C cathode of the cycled battery. The characteristic peaks of Co_3S_4 and Co_4S_3 are recognized in the patterns at different states. indicating the formation of cobalt polysulfides in the initial cycles at both the discharged and charged states. The formation of cobalt polysulfides should be responsible for the rapid capacity decline in the initial few cycles.

Recently, many types of transit metal-based materials have been extended their applications to Al–S batteries depending on their high affinities to sulfur species and potential catalytic capability. Wang and co-workers[12a] have reported a bifunctional TiN-N-doped-graphene (TiN-NG) catalyst for reversible Al–S batteries. As presented in Figure 4G, the TiN-NG composite powder was incorporated into sulfur cathodes to suppress the shuttle effects in virtue of the strong chemical adsorption of TiN and NG toward polar polysulfides. At the same time, sulfide redox kinetics are promoted and the decomposition reaction barrier is reduced by the activation sites of TiN. The absorbance for the solution after soaking the TiN-NG catalyst powders is near zero and the binding energy of Ti 2p peaks and N 1s peak shift after adsorption, confirming that the polysulfide molecules have been interacted with the TiN-NG. Meanwhile, the electrolyte in a TiN-NG:S//Al transparent cell with no obvious color variation during the whole discharging–charging process also witnesses the strong ability in suppressing the shuttle effect of polysulfides (Figure 4H). In the CV curves, the TiN-NG:S cathode displays higher peak current and higher slope, indicating the enhanced polysulfide conversion kinetics (Figure 4I). To make the Al–S electrochemistry clearer, the valence state changes and aluminum storage mechanisms in sulfur cathodes during charge and discharge were recorded and analyzed by ex situ XPS and EDS mappings. In detail, the valent evolution of the S 2p spectra from the initial to discharged, finally to charged state indicates the reverse redox conversion from S_8 to long-chain polysulfides and to short-chain polysulfides. Meanwhile, the evolution of the Al 2p spectra during this process also confirms the motion law of Al^{3+} ions between the cathode and electrolyte. That is the aluminum-enriched condition in the discharged sulfur cathode, and the aluminum absent state after releasing back to electrolyte in the charge process, which is verified by the subsequent SEM and EDS mapping images in Figure 4J. These fully suggest the catalytic role of TiN in reducing the polarization and reaction barrier of the Al–S electrochemistry.

Although the viable catalyzing effect of the metal–base catalysts is developed for Al–S systems, the catalytic activity is unsaturated and still far behind the demand to boost rate performance and lifespan. As far as we know, more active sites will benefit higher catalytic excitability.[1e,2h] If the particle size of catalyst is

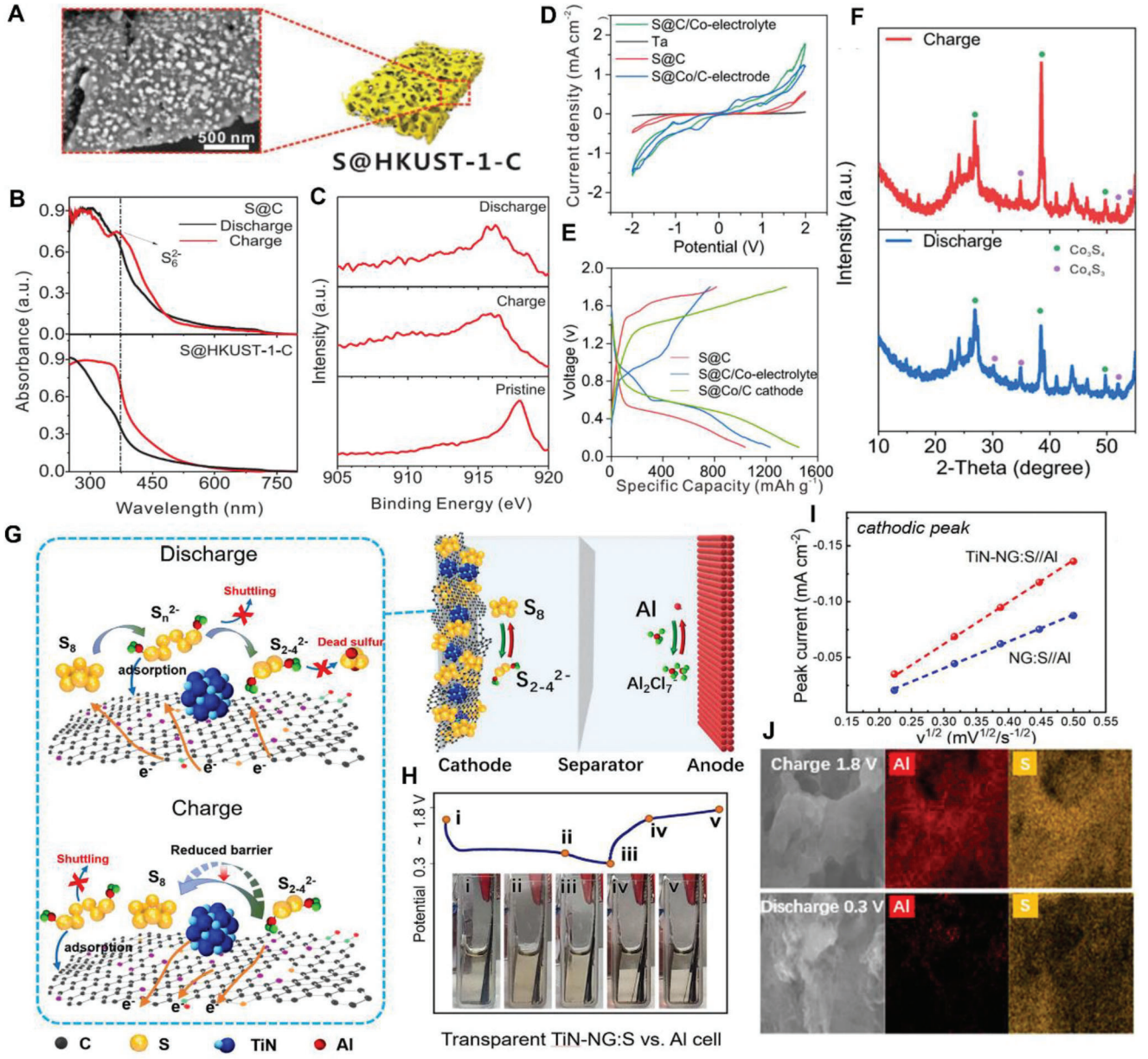

Figure 4. A) Schematically illustrating the sulfur infiltrated copper nanoparticle-decorated microporous carbon. B) UV–vis absorption spectra of the separator in Al–S battery with cathodes of S@HKUST-1-C and S@C. C) Cu LMM auger spectra of Al–S battery cathode under different charge states; Reproduced with permission.[31] Copyright 2019, Wiley-VCH GmbH. D) Symmetric cells CV profiles on the three symmetric cells. E) Galvanostatic discharge–charge curves at the initial cycle measured at a current density of 1 A g^{-1}; F) XRD patterns of the S@Co/C cathode at the discharged and charged states; Reproduced with permission.[11a] Copyright 2020, Wiley-VCH. G) The configuration and working principle illustration of the TiN-NG:S//Al batteries. H) Optical photo of the transparent TiN-NG:S//Al cell at different charging-discharging stages. I) Plot of the cathodic peak currents versus the square root of the scan rates. J) SEM images and EDS mapping of the cathode from the cycled TiN-NG:S//Al batteries at different charge and discharge stages. Reproduced with permission.[12a] Copyright 2022, Elsevier.

decreased to the monodispersed atomic level to form the so-called single atomic catalysts (SACs), the utilization of the metal atoms would realize the maximum level to gain the highest reactivity at the expense of merely little energy density.[32] In view of this, single atomic catalysts (SACs) with unique superiority open the access to high efficiency catalysis in Al–S systems and have obtained many recent focuses.

Ji's group proposed a single-atom catalysts comprising Co atoms embedded in a nitrogen-doped graphene (CoNG) for the sulfur cathode of Al–S systems.[12d] It is confirmed that Co atoms are coordinated to N atoms to form Co–N_4 coordination centers, rendering a reduced discharge–charge voltage hysteresis and improved sulfur utilization in the cathode. Therefore, a kinetically accelerated Al–S battery assembled with CoNG-S

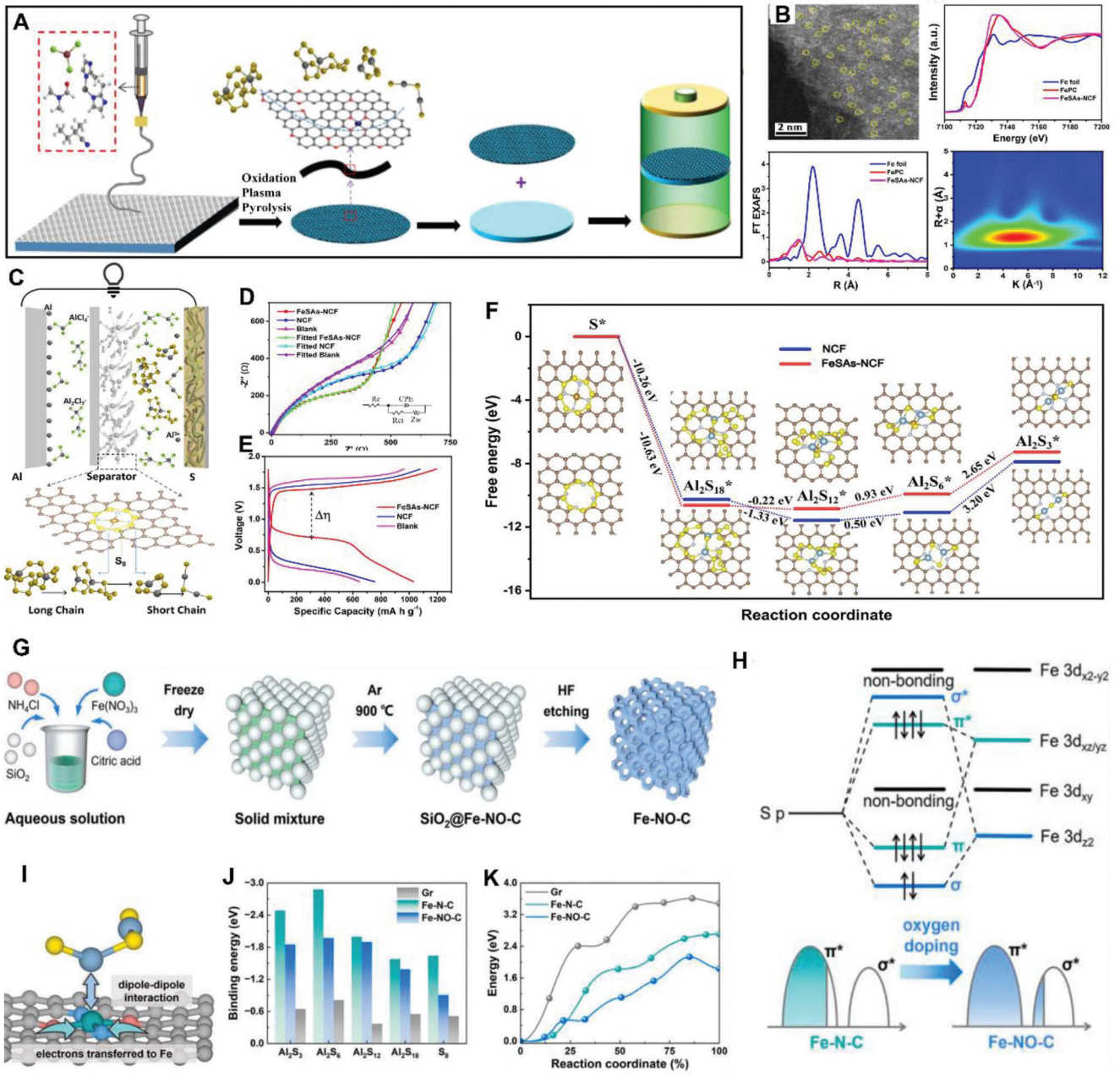

Figure 5. A) Synthetic illustration of the synthesis process of FeSAs–NCF nanostructure. B) Aberration-corrected HAADF-STEM image, XANES, Fourier transformed EXAFS spectra, and wavelet transforms of the FeSAs-NCF. C) Schematic description of inhibiting shuttle effect and catalyzing sulfur species in the Al–S battery with FeSAs–NCF. D) Nyquist plots and E) charge–discharge curves of the Al–S batteries with FeSAs–NCF nanocatalyst. F) Energy comparison for the reduction of sulfur to aluminum sulfides on NCF and FeSAs–NCF; Reproduced under the terms of the Creative Common CC BY license.[33] Copyright 2022, The Authors, published by Springer. G) Schematically illustrating the preparation of S@Fe–NO–C. H) The d–p orbital hybridization scenario between Fe–N–C and metal sulfides, and conceptual illustrations of the d–p orbital hybridized density of states for Fe–N–C and Fe–NO–C with sulfur species adsorption. I) Schematic illustrations of the charge transfer and interaction patterns in Al_2S_3@Fe–NO–C. J) Comparison of binding energies and K) decomposition energy barriers for Al_2S_3 molecule on Fe–N–C and Fe–NO–C. Reproduced with permission.[34] Copyright 2023, Elsevier.

cathode yields a gravimetric capacity of 1631 mA h g^{-1} with a sulfur utilization of more than 97% and a low voltage hysteresis of 0.76 V. Inspired by this SACs enhanced Al–S electrochemistry, an interconnected free-standing interlayer composed of SACs with distinctive electronic structure on the separator is proposed by Fu and co-workers.[33] In this design, iron single atoms supported on porous nitrogen-doped carbon nanofibers (FeSAs-NCF) with free-standing network are fabricated and directly coated onto the separator to form the interlayer (**Figure 5**A). The atomically dispersed iron active sites were clearly identified

by aberration-corrected high-angle annular dark-field scanning transmission electron microscopy (HAADF-STEM) and X-ray absorption near-edge structure (XANES). The Fe single atoms are clearly identified throughout the carbon nanofibers in the enlarged HAADF-STEM image (Figure 5B). The Fe K-edge XANES spectra confirm the Fe–N coordination in the FeSAs–NCF composite. The Fourier-transformed (FT) k^2-weighted-EXAFS spectra are further fitted to identify the coordination number of Fe. The calculated coordination number of Fe–N is ≈3.52 in the first shell of Fe atoms for FeSAs–NCF, demonstrating that the Fe is atomically dispersed and coordinated with N as Fe–N_4. The wavelet transform-EXAFS (WT-EXAFS) contour plot of the FeSAs–NCF is also described, further confirming the Fe–N coordination (Figure 5B). This well-designed catalytic structure cannot only physically block soluble aluminum polysulfides and chemically interact with aluminum polysulfides to suppress the shuttle effect, but also accelerate the charge transfer and reaction kinetics (Figure 5C,D). As a result, the cell with FeSAs–NCF shows a higher discharge capacity of 1130 mA h g^{-1} at current density of 100 mA g^{-1} and possesses a lower electrochemical polarization than the controlled cells, indicating the decreased energy barrier of the conversion reactions (Figure 5E). To further discover the improved reaction kinetics of the aluminum polysulfides, the overall reductions from S_8 to Al_2S_3 involved in multiple intermediates including Al_2S_{18}, Al_2S_{12}, and Al_2S_6 during the discharge were simulated via first-principal theory calculations (Figure 5F). The theoretical calculation discovers that the formation of Al_2S_3 from Al_2S_6 has the largest positive Gibbs free energy, indicating the rate-determining step of this process among the entire conversion reactions. For the reaction of Al_2S_6, the Gibbs free energy on the FeSAs–NCF (2.65 eV) is lower than that on the NCF (3.20 eV), which demonstrates that the reduction of S is thermodynamically more favorable on the FeSAs–NCF than on the NCF substrate.

As well known, heteroatom doping is one of the most effective optimization methods to modulate electronic density and chemical absorption ability. Relying on the coordination with variety of heteroatoms (such as N and O), the metallic single atoms would be anchored with unsaturated electronic structures on the nanocarbon to acquire different catalytic effect.[1e] To this end, N, O dual-coordinated single-atom iron catalysts (Fe–NO–C) were exemplified and developed by Yu's group to unravel the influence of coordinating oxygen on catalytic efficiencies for Al–S batteries (Figure 5G).[34] Upon the comparison of the N, O dual-coordinated sites (Fe–NO–C) with nitrogen moiety (Fe–N–C), Figure 5H depicts the orbital rearrangement and charge filling in the charge transfer derived from d—p hybridization. The S p orbitals hybridize with Fe d-orbitals, forming bonding states (σ and π), anti-bonding states (σ^* and π^*) and nonbonding states. As discussed in the literatures, the low-energy bonding states are fully occupied and anti-bonding states are filled partially for Al_2S_3@–Fe–N–C. And the enhanced antibonding states for Al_2S_3@–Fe–NO–C depress the d–p hybridization. If the Fe–NO–C interacts with Al_2S_3 molecule in an Al-binding configuration, the catalytic center would be polarized by the Al_2S_3 to withdraw electrons from the π-conjugated system via inductive effect (Figure 5I). The presence of high electronegative oxygen in the coordination environment reinforces the inductive effect so that more electrons are attracted to the catalytic center Fe to enhance the electrostatic interaction between Al_2S_3 and Fe–NO–C, resulting in a tiny reduce in the binding energy to the sulfur species (Figure 5J). Thanks to such depressed d–p hybridization, the dissociation energy barriers of Al_2S_3 molecules are decreased from 2.72 eV on Fe–N–C to 2.13 eV on Fe–NO–C (Figure 5K) and the relative free energy for the discharge process is also lowered due to the optimized reaction pathways. Following above design principles, the Al–S electrochemistry with Fe–NO–C is kinetically enhanced than that on the Fe–N–C. The as-synthesized S@Fe–NO–C cathode in Al–S cells displays impressive rate performance (352 mA h g^{-1} at 3 A g^{-1}) and excellent cycling stability (550 mA h g^{-1} after 400 cycles).

As the applications of SACs in lithium–sulfur batteries move on, the diverse SAC categories do play a critical role in promoting catalytic efficiencies and electrochemical properties. Yu et al.[35] compared the catalytic activity of different transition metallic SACs interacting with a nitrogen moiety in porous carbon for Al–S batteries, denoted as SATM@NC (TM = Ti, V, Cr, Mn, Fe, Co, Ni, Cu). The five representative SATM@NC (TM = Mn, Fe, Co, Ni, Cu) catalysts with similar morphology and loading were synthesized by a universal method in **Figure 6**A from chemical vapor deposition (CVD) to MOF derivation. Through the cyclic stability of the sulfur cathode with SATM@NC, the Al–S cell based on SACo@NC maintains the highest discharge specific capacity of 567 mA h g^{-1} after 100 cycles, demonstrating the best catalytic activity of atomic Co site among the various SATM (Figure 6B). Combining with the DFT results, all the SATM@NC composites show remarkable catalytic effects on the conversion reactions. Atomic metal species increase the reactivity of aluminum polysulfides (AlPSs) through weakening the Al–S bonds. Among them, the distinctive binding interaction between AlPSs and SACo@NC is critical for its superior catalytic activity. Hence, SACo@NC is regarded as the most promising catalyst, which exhibited the lowest Gibbs free energy for the rate-dominating reaction steps of sulfur reductions and the lowest barrier (2.45 eV vs 2.7–2.9 eV) for Al_2S_3 decomposition (Figure 6C).

From the above works, it is easy to find the accessibility of theoretical calculations in guiding the precise designs of SACs. In order to meet the practical demands in devices, more and more SACs need to be screened and compared in the Al–S battery systems. Combination of experiment analysis with theoretical computation manners becomes a viable and vital pattern to open the in-depth understanding in the structure–function relationships of SACs, and effectively reduce the number of unsuccessful trials to simplify the experimental steps at the same time.[12b,g,36] Making the full use of theoretical simulation tool, Wei and co-workers carried out the theoretical modeling to screen the potential SACs candidates and decipher the interaction mechanism between Al_2S_n and SACs. Single-atom-loaded MXene (SA@MXene) is used as a representative anchoring material to systematically simulate the binding strength between SA@MXene and Al_2S_n, and the energy barriers faced by sulfur reduction process on MXene.[8c] Figure 6D shows the 20 kinds of transition metal (TM) atoms including 3d- and 4d-TM atoms. Taking an overall consideration from the scarcity, toxicity, and the formation energies (E_f) of SA@$Ti_3C_2O_2$ structures, eight types of SA@$Ti_3C_2O_2$ (SA = Zr, Nb, Y, Sc, Mo, Tc, V, and Cr) with a low E_f may be favored by experimental researchers. Then, an adsorption energy

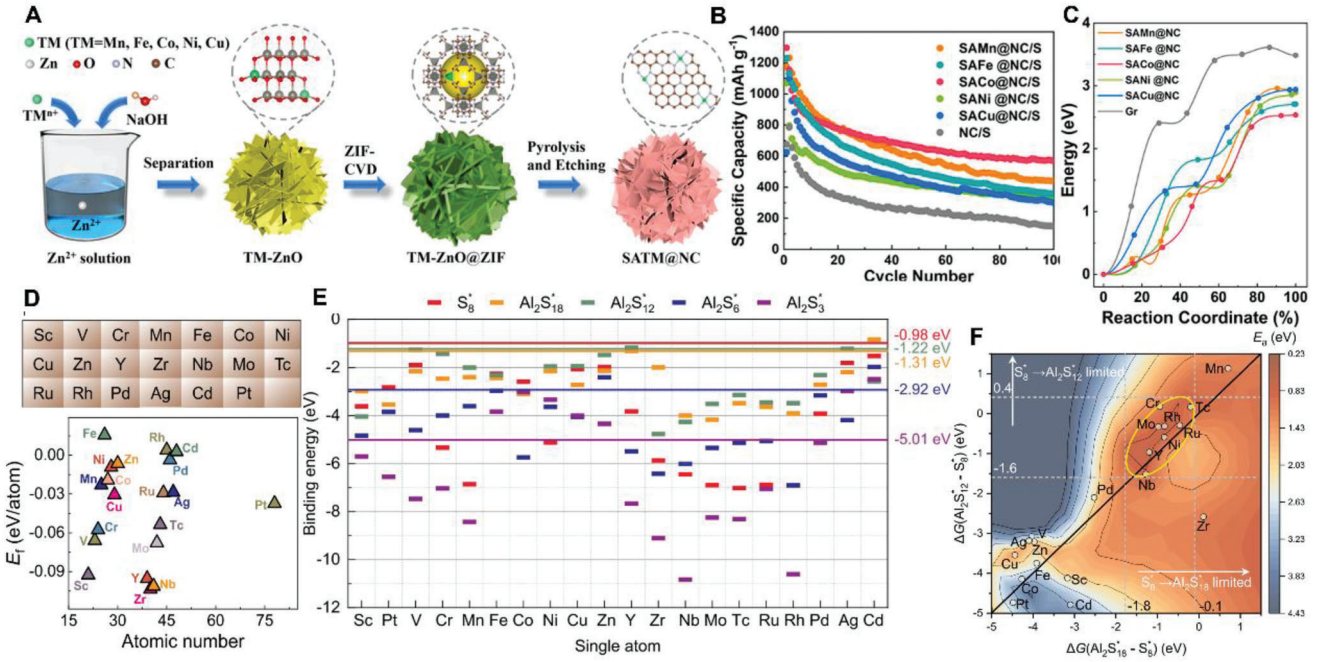

Figure 6. A) Schematic description of the universal synthesis of SATM@NC nanocomposites. B) Cyclic performance of SATM@NC/S cathodes. C) The energy curves for the decomposition of Al_2S_3 on SATM@NC. Reproduced with permission.[35] Copyright 2022, Elsevier. D) Choices of TM atoms and the corresponding formation energies of SA@$Ti_3C_2O_2$ structures. E) E_b values of S_8 and Al_2S_n species on SA@$Ti_3C_2O_2$ nanosheets. F) Activity volcano determined by ΔG (Al_2S_{18}*–S_8*) and ΔG (Al_2S_{12}*–S_8*). Reproduced with permission.[8c] Copyright 2022, American Chemical Society.

(E_b) map of the 20 TM atoms is simulated (Figure 6E). The E_b values of S_8*, Al_2S_{18}*, Al_2S_{12}*, Al_2S_6*, and Al_2S_3* on pristine $Ti_3C_2O_2$ (−0.98 eV, −1.31 eV, −1.22 eV, −2.92 eV, and −5.01 eV) are set as the selecting criterion for screening. In this way, around fourteen types of SA@$Ti_3C_2O_2$ nanosheets (SA = Sc, Pt, V, Cr, Mn, Y, Zr, Ti, Nb, Mo, Tc, Ru, Rh, and Pd) are preferentially selected and are of great experimental interest. Afterward, the Gibbs free energy profile including all the intermediates based on the complete reaction paths of S_8 and Al_2S_n species is also theoretically described. Through a systematically simulation on the free energy differences (ΔG), an activity volcano determined by ΔG(Al_2S_{18}*–S_8*) and ΔG(Al_2S_{12}*–S_8*) is depicted, which could be used to estimate the whole reaction kinetics and unravel the interaction mechanism between Al_2S_n and the anchoring materials (Figure 6F). After a comprehensive assessment on the energy barriers with respect to various stepwise sulfur interconversions on the different SA@MXene nanosheets, four high-performance catalyst candidates for Al–S batteries (SA = Y, Nb, Mo, Tc) with a minimum reaction energy barrier ≈0.23 eV are screened out. This theoretical work provides a significant roadmap to guide the SACs design rules and enlighten the importance of artificial intelligence in Al–S batteries.

2.4. Robust Functional Covalent Polymers for Binding Sulfur Related Species

As we all know that polymers could change different functional groups in the ligand or skeletons. Incorporating sulfur chains into the conductive polymers seems be feasible, which allows the effective accessibility of ions and electron and the sequestration of the formed polysulfides to improve the reversibility of the cathodes.[12e,37]

Inspired by the effect of rubber vulcanization, sulfurized polyacrylonitrile (SPAN) as a typical sulfur-containing compound was applied in Al–S battery by Ming's group to investigate the relationship between polymer molecular structures and electrochemical mechanisms, interpreting the electrochemical behaviors in organic polymer–sulfur systems.[38] With the help of ex situ electron paramagnetic resonance (EPR) spectrum, it is found that the signal of thiyl-based radical appears and the intensity fluctuates repeatedly at the state of different (dis-)charge behaviors in **Figure 7**A. The radical intensity increased initially as the continuous S–S cleavage, while it weakens when the chemical combination of radicals with Li^+ after the coupling electron occurs in the further discharge state. Reversibly, the radical signal rises again as the radical with Li^+ extracting from the SPAN structure when the battery is recharged and then maintains stable existence in the following charge process. A possible evolution of the SPAN structure is presented in Figure 7B. Starting from the pristine SPAN, radical SPAN become linear and converts to a "zigzag" shape ionic SPAN subsequently when accepting electrons from the external circuit. This kind of molecular structure has a large space with negative locations, enabling the molecules to obtain high activity to react with Li. On the basis of the above analysis, speculated molecular structure is confirmed again by ex situ XPS analysis in Figure 7C. It is uncovered that the conjugative structured thiyl radical prefers to maintain the intermediate framework, rather than reconnection to form a S–S bond after the first cycle due to the stabilization effect of the

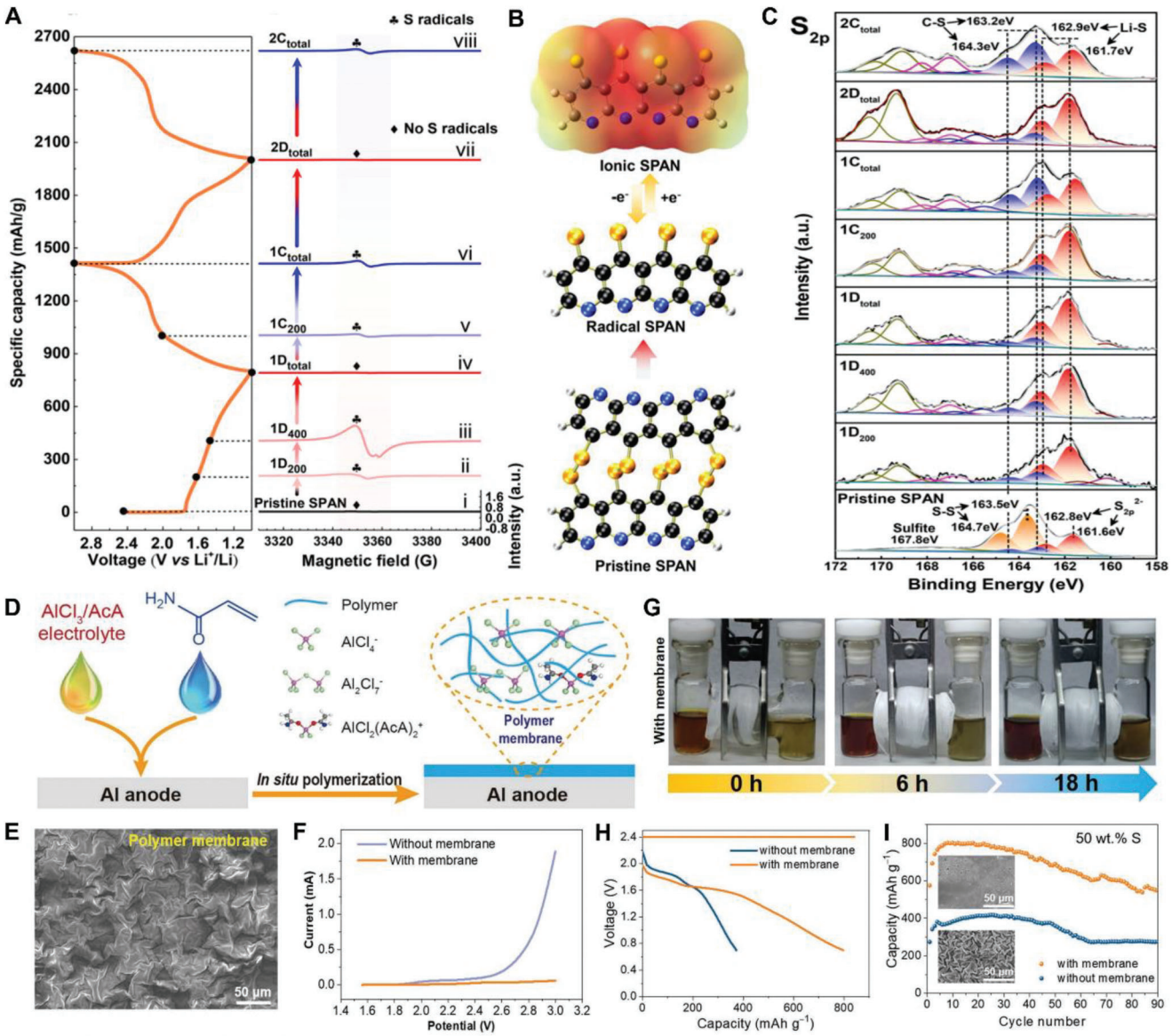

Figure 7. A) Galvanostatic (dis-)discharge curves of SPAN in the first and second cycles and the corresponding ex situ EPR spectra. B) Proposed structural evolution from pristine SPAN to the intermediates of radical and ionic SPAN in the reactions. C) High-resolution ex situ X-ray photoelectron spectroscopy (XPS) spectra of S 2p for SPAN at different discharge and charge states. Reproduced with permission.[38] Copyright 2018, American Chemical Society. D) Schematic illustration of the in situ fabrication of polymer membrane. E) SEM image of the modified membrane on the Al foil. F) LSV profiles obtained on Mo–Al batteries using Al foils without and with membrane. G) The diffusions process of soluble sulfur species in the H-type cells with polymer membrane. H) Potentiostatic charge and galvanostatic discharge curves of Al–S batteries with and without the polymer membrane. I) Cycle performance of the Al–S battery with/without the modified membrane. Reproduced with permission.[8f] Copyright 2022, Wiley-VCH GmbH.

conjugated π-accepting group, facilitating the reaction with lithium ions through a Li-coupled electron transfer process and forming an ion-coordination bond reversibly. This clearly unveils the real reason for the superior lithium storage capability, in which the lithium polysulfide is resisted from formation. As expected, such cognition also successfully guides an access to get high performance in Al–S battery applications.

On the other hand, introducing versatile polymer as membrane on the anodic side against the direct contact between sulfur species and metallic Al is also a wise strategy. Since the liquid-phase sulfur species could easily diffuse from cathode to anode side, Yu et al. fabricated a polyacrylamide membrane infiltrated with ≈50 wt% $AlCl_3$/AcA electrolyte on the surface Al foil anode (Figure 7D), separating the Al from polysulfides.[8f] With this in situ polymerization, a corrugated texture in Figure 7E is formed on the Al foil with some cracking lines to facilitate the ion transport from/to the Al anode. As shown in the linear sweep voltammetry (LSV) profiles (Figure 7F), it is found a fast current increase starts from ≈2.4 V in the absence of the membrane while the onset voltage of the electrolyte electrochemical oxidation is

significantly increased with membrane, suggesting the unexpected electrochemical oxidation reactions of the $AlCl_3$/AcA electrolyte are suppressed. The suppression of these side reactions might be attributed to the reduced local concentration of electrolyte after membrane regulation, which is also beneficial to the efficient activation of sulfur. At the same time, the amide groups in the polymer chain can facilitate the enhanced adsorption of ions of electrolyte by chemical coordination. The role of the polymer membrane on inhibiting the shuttle effect is then monitored in a H-type cells (Figure 7G). With the membrane covering on the separator, this diffusion of sulfur species is noticeably slowed down in comparison with that in the membrane-absence one. As a result, the capacity with membrane protection (Figure 7H) is enhanced nearly two times (380 vs 800 mA h g^{-1}), and the electrochemical stability of the as-fabricated Al–S battery is improved with a high-capacity retention of 86% after 50 cycles (Figure 7I).

3. Electrolyte Designs for Recyclable Aluminum Batteries

Aside from the aforementioned cathode configurations to prohibit polysulfide shuttling, another ubiquitous and indispensable component to push the rechargeable Al-based batteries to a higher level is the choice of compatible electrolytes.[21a,39] As a matter of fact, the electrolytes for Al–S batteries are not as mature as the Li–S batteries because that rechargeable aluminum–sulfur batteries are still at their attempt stage. As expected, the higher ion transportation in the electrolyte with low viscosity is beneficial for achieving high-performance Al–S batteries. In views of recent developed electrolytes, they can be classified into three main types:[19a,b,40] i) inorganic melt salt system; ii) aqueous electrolyte; iii) room temperature ionic liquid based organic electrolyte.

3.1. Temperature-Relied Inorganic Melt Salt System

In the early stage, a typical Al–S battery system was first reported by Marassi's group in which $AlCl_3$–NaCl melts were employed as the electrolyte.[15] The operation of the $AlCl_3$–NaCl melts should be performed in the high temperature. In this work, it is demonstrated that the sulfur is electrochemically active and workable. However, the voltage hysteresis of the fabricated cell is greatly dependent on the cycling temperature. The reduction of sulfur results in the formation of sulfide, while conversely the oxidation state to S (I) or S (II) significantly relies on the temperature. That means the higher oxidation state needs to be operated at higher temperature. Apparently, the mechanism for the electrochemical redox reactions of sulfur involves in a divinable set of charge/mass transfer kinetics related to temperature. Subsequently, Osteryoung's team discovered that the electrochemical equilibrium formed in the acid and basic $AlCl_3$–NaCl melts at 175 °C, involving sulfides and the solvent in the Al–S electrochemistry: $AlCl_4^- + S^{2-} \rightarrow AlSCl + 3Cl^-$. This can be directly corroborated from the CV of sulfur and sulfide in the melt electrolyte. The cathodic waves in the CV curves around ≈1.5 V and 1.0 V are assigned to the reduction of S formed at the electrode surface during the initial anodic scan. The reverse anodic peak at ≈2.2 V is ascribed to the oxidation from S^{2-} to S. Combining these investigations provided by Marassi and Osteryoung's groups,[15,41] it is easy to conclude that the electrochemical activity of sulfur in the $AlCl_3$–NaCl melts is heavily dependent on the temperature range of the cells, indicating that there is still a long road for the follow-up researchers to go from starting the electrochemical activity to fulfill a real rechargeable Al–S cell with $AlCl_3$–NaCl related electrolyte.

3.2. Low-Cost Aqueous Electrolyte

Since 1993, in order to quest for a more feasible and stable electrochemical reaction of S with Al at room temperature, Al–S batteries with aqueous electrolytes, partially reversible Al plating and stripping were developed. On the other hand, the developmental advantages including low cost, easy to made, and environmental friendliness of aqueous electrolytes make them quite viable alternatives to design and assemble Al–S batteries. In the aqueous electrolytes, the carriers will be OH^- species and the Al–S batteries deliver the following main reaction process: $2Al + 3S + 3OH^- + 3H_2O \rightarrow 2Al(OH)_3 + 3HS^-$, as explored and reported by Licht's team.[12f] Although the theoretical energy density of this water-based Al–S battery was as high as 910 W h kg^{-1}, there are still many drawbacks such as the oxidative passivation layer formation on the Al surface and side reactions of hydrogen evolution reaction existing in this battery system, directly leading to an anodic efficiency as low as 45% and obvious anodic overpotential enlargement at a current density of 0.2 mA cm^{-2}. According to the electrochemical reaction mechanism raised by Licht's team, the final discharge product of the Al–S system in the alkaline aqueous electrolyte is revealed as $Al(OH)_3$, which is too stable to be reduced back to aluminum metal, further limiting the development of aluminum secondary batteries.[42] Thereby, it is extremely challenging for researchers to continuously look for new and more suitable aqueous electrolytes to overcome these scientific challenges and further construct cyclable reversible/rechargeable Al–S batteries.

To rule out the formation of insoluble Al-based oxides or hydroxides, one can easily think about the introduction of slight acid into the system. Recently, Hu et al.[43] successfully put forward an acid activation aqueous electrolyte to develop a rechargeable Al–S battery with the configuration of $Al \| Al(OTF)_3$ + LiTFSI+ HCl ‖ S/C. It is worth noting that the super-concentrated LiTFSI traps water molecules to inhibit the hydrolysis of aluminum polysulfides in the cathode, and the HCl additive provided a mild acidic environment to prevent the formation of a passivation layer on the Al anode surface and enabled the smooth going of reversible oxidation–reduction reactions. Thanks to this updated electrolyte composition, the aqueous Al–S battery delivered a high initial capacity of 1410 mA h g^{-1} and maintained a reversible capacity of 420 mA h g^{-1} after 30 cycles with a relatively high Coulombic efficiency of 97%. However, future investigation directing at the large voltage hysteresis and low cycle stability still needs to be addressed in the aqueous electrolyte systems.

3.3. Highly-Reversible Ionic Liquid System

Ionic liquids, being known as a unique class of materials, consisting of organic cations and inorganic/organic anions, have been

widely applied in nonaqueous Al-based batteries to further improve the interfacial properties and obtain high reversible stripping/plating behaviors of aluminum metal.[13a] In recent years, room-temperature ionic liquid as electrolyte for Al–S battery is put forward due to a sequence of attractive properties, such as ionic conductivity, ultralow volatility, good thermal stability and low flammability, less possibility of side reactions, offering more probability of enhanced safety and stability to Al–S secondary batteries.[13b,17a,23a]

In most cases, researchers are mainly devoted to develop ideal electrolytes with high ionic transport ability, good electrochemical stability to improve the capacity, prolonging cycling life, and improving battery safety when cycling.[23a] By means of the low stability of the ion-solvent complex, the ionic liquids contribute to a rapid solvation/desolvation of aluminum ion, allowing superior transport kinetics to the other types of electrolytes during the electrochemical reaction. The main reaction process of the Al–S battery based on the current ionic liquid electrolyte systems can be described as $2Al + 3S \rightarrow Al_2S_3$. In this battery system, the theoretical specific capacity is much boosted to surpass 1000 mA h g^{-1}, with the energy density exceeding 1200 W h kg^{-1}, while the theoretical voltage is calculated to be 1.3 V upon Gibbs free energy.[8d,12b]

In this view, the breakthrough in the capacity and reversibility with ionic liquids is far beyond the previous Al–S based batteries with inorganic melt and aqueous electrolyte systems.[19a] Instead of high-temperature molten salt or water-in-salt electrolytes, a growing interest is focused on developing long-chain imidazolium ionic liquid as electrolytes, such as $AlCl_3$+EMICl (1-ethyl-3-methyl-imidazolium chloride) and $AlCl_3$+[BMIM]Cl (1-butyl-3-methyli-midazolium chloride),[8d,12b] for high-performance Al anode-based batteries in recent few years. With the action of the alkyl segments, the long-chain imidazolium as organic cations in this $AlCl_3$+EMICl electrolyte is beneficial for boosting the affinity of ionic liquids to inorganic and organic materials, resulting in meliorative interfacial contact properties to expand the materials diversity in cathode design and Al-anode modulation. Thereby, a series of mole ratios between $AlCl_3$ and imidazolium chloride was comprehensively studied by Wu' group,[13b] aiming to reveal anion effects on ionic liquid properties and rechargeable aluminum battery performance. It was unveiled that the electrochemical window and conductivity of ionic liquids are affected by the aluminum chloride anions ($Cl^- \rightarrow AlCl_4^- \rightarrow Al_2Cl_7^-$) resulting from different $AlCl_3$/imidazole salt mole ratios, which is the determinant step in the electrochemical activities. Through the combination of theoretical calculation with electrochemical analysis, it is found that the concentration of $Al_2Cl_7^-$ is considered as a key factor to the rechargeable reversibly charge/discharge performance. When the battery employs with the $AlCl_3$/[BMIM]Cl = 1.1:1 ionic liquid as the electrolyte, a proper $Al_2Cl_7^-$ concentration results in a slightly pitting corrosion on the Al metal anode, which is beneficial for wiping off the oxide passivation film on Al metal foil and promoting the reversibility of aluminum metal anode.

Then, Cohn et al. introduced the long-chain imidazolium ionic liquid of $AlCl_3$+EMICl as the selected electrolyte coupling with the sulfur cathode and aluminum anode to assemble a novel Al–S battery.[6a] Consequently, the Al–S battery delivers an initial capacity as high as 1400 mA h g^{-1}, more than 80% of the theoretical capacity for a sulfur-based cathode system. In a deep interpretation, the electrochemical reduction of elemental sulfur changes significantly while varying the ratio between $AlCl_3$ to EMICl ratio. $AlCl_4^-$ ions have been recognized as the electroactive ionic species during the entire redox process. However, there is a "trade-off" of the concentration of $AlCl_4^-$ ions in the electrolyte because the presence of too much $AlCl_4^-$ ions in the electrolyte will prevent the electrodeposition of Al during charging/discharging, compromising the merits of discharge effectiveness and recharge capabilities. Furthermore, as the increase of the CV scan rate, it is found that the conversion reaction is determined partly by the kinetics of charge transfer and partly by diffusion of electroactive species $AlCl_4^-$, implying the possibility of enhancing the reaction kinetics through modulating the electrolyte composition in the ionic liquid systems.

Apart from enhancing the reaction kinetics via tuning electrolyte ratio, another intriguing function of the imidazolium ionic liquid is serving as an inhibition agent to resist the dendrite growth on the Al anode surface. According to Manthiram's viewpoint[13d] presented in **Figure 8**A, the Al anode reaction during the discharge–charge in an Al–S cell is supposed to be a reversible process as: $Al + 7AlCl_4^- \leftrightarrow 4Al_2Cl_7^- + 3e^-$. During charging process, electrons migrate from the oxidation of Al_2S_3 species in the cathode (the S electrode) to the anode (Al electrode) through the external circuit. The $Al_2Cl_7^-$ species at the anode then accept electrons to dissociate as Al and $AlCl_4^-$, plating on the Al surface. In order to keep a closed circuit, the $Al_2Cl_7^-$ species migrate from the cathode side to the anode side inside the cell. The discharge then experiences a reverse process. Unlike the anode chemistries of Li and Na, using the imidazolium ionic liquid to enhance the transportation of larger ionic size of $Al_2Cl_7^-$ species is likely to boost the kinetics of the cell reaction. Meanwhile, due to the existence of larger ionic size of $Al_2Cl_7^-$ and $AlCl_4^-$ species at the anode side, the deposition/striping quality in the Al–S cell tends to be interfered easily.

To reach this goal, the deposition/striping regulation in the Al–S cell is expected to be as prominent relative to the electrochemical performance as those in the Li–S cells. Therefore, Gao et al.[6b] reported a reversible Al–S battery in $AlCl_3$ + EMICl ionic liquid electrolyte with an activated carbon cloth/sulfur composite cathode. Distinctive from typical Li–S battery system, a solid-state conversion reaction of sulfur to aluminum sulfide is confirmed through measuring the solubility of different sulfur species in the ionic liquid electrolyte (Figure 8B). It is revealed that aluminum polysulfide ($Al_{2/3}S_6$) and aluminum sulfide (Al_2S_3) have similar low solubility (very slightly soluble) in this type of ionic liquid electrolyte. Due to the low ion mobility, the first hurdle for oxidization of AlS_x is addressed through confining sulfur species into microporous carbon to improve the electron accessibility of sulfur species, enlarge the interfacial reaction area, and reduce the Al^{3+} diffusion length to the sulfur species. In the oxidization process, the readiness to oxidize AlS_x and low sulfur loss into the electrolyte bring about a substantially improved reversibility with a high capacity of 1000 mA h g^{-1} over 20 cycles. On the other hand, the excellent reversibility should be attributed to the free of dendrite on the Al anode within the whole cycling process. The aluminum plating/stripping and the anodic stability of the electrolyte on glassy carbon were given in the Al stripping/plating curves, as shown

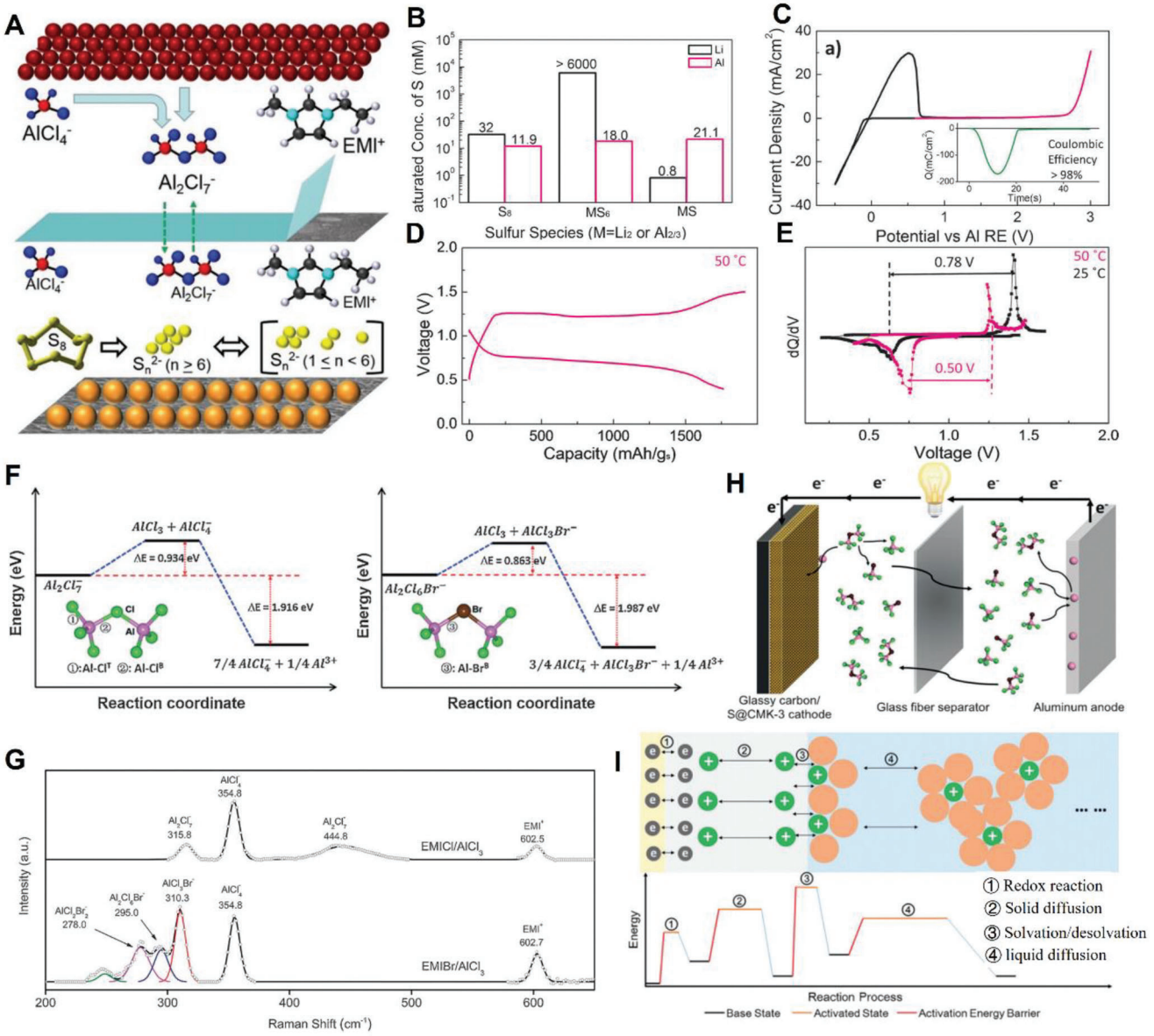

Figure 8. A) Description of the electrochemical discharge–charge mechanism of the Al–S batteries with ionic liquid. Reproduced with permission.[13d] Copyright 2017, Wiley-VCH GmbH. B) Solubility of different sulfur species in Li and Al related electrolytes. C) Al deposition/striping in EMIC:$AlCl_3$ = 1:1.3 electrolyte (black) and the electrochemical stability of the electrolyte (pink). D) Charge/discharge profile at 50 °C. E) The dQ/dV curves of Al–S cells under different temperatures. Reproduced with permission.[6b] Copyright 2016, Wiley-VCH GmbH. F) Energy profiles of the dissociation reactions with $Al_2Cl_7^-$ and $Al_2Cl_6Br^-$ electrolyte. G) Raman spectra of EMIBr/$AlCl_3$ and EMICl/$AlCl_3$ electrolytes. H) The discharge process of an Al–S battery with NBMPBr/ $AlCl_3$ electrolyte. I) A representation of the relationship between activation energies and electrochemical processes. Reproduced with permission.[8d] Copyright 2018, Wiley-VCH GmbH.

in Figure 8C. With the $AlCl_3$+EMICl ionic liquid electrolyte, the deposition of Al occurs through the decomposition from $Al_2Cl_7^-$ to $AlCl_4^-$ and Al, which starts at low over-potential and proceeds at very fast kinetics (-30 mA cm^{-2} at −0.5 V in Figure 8C). Charge balance curve (the inset of Figure 8C) shows the deposition/stripping process is highly reversible with a Coulombic efficiency close to 100%, which is the premise of the dendrite-free deposition/striping at the Al anode in this Al–S system. However, a large voltage hysteresis (0.78 V at 50 mA g^{-1}) was still observed during charge/discharge, which leads to a low roundtrip efficiency of the Al–S cell. This overall voltage loss should be ascribed to the main contribution of the sluggish cathode charge transfer in the solid-state sulfur conversion reaction, which could be explained by elevating the temperature that the large voltage hysteresis can be effectively reduced to 0.5 V as observed from the voltage profile and$Q$/dV curve in Figures 8D and 8E, respectively.

In addition, it is also easy to see that the formation/dissociation reaction in the Al–S electrochemistry mainly occurs in the interface between the cathode/anode and electrolyte. Enlightened

from the Li–S and Na–S electrochemistry, electrolyte makes great contribution to modulate the interfacial reactions kinetically. Li's team had innovatively substituted the $Al_2Cl_7^-$ for $Al_2Cl_6Br^-$ as the dissociation reaction reagent in the 1-ethyl-3-methylimidazolium chloride (EMICl) ionic liquid to alter the interfacial state between the cathode and electrolyte, leading to some new discoveries.[8d] As displayed in Figure 8F, the energy barrier for $Al_2Cl_6Br^-$ dissociation is lowered by 71 meV per molecule (that is, 6.8 kJ mol^{-1}) than that for $Al_2Cl_7^-$, implying that the interfacial reaction relating to the dissociation of $Al_2Cl_6Br^-$ is energetically easier than that of $Al_2Cl_7^-$. It is calculated to be a 15 times faster dissociation reaction rate based on the Arrhenius equation. Liquid Raman spectroscopy in Figure 8G was applied to experimentally identify possible ions in these two different electrolytes. After electrolyte modification, three new peaks in the EMIBr/$AlCl_3$ electrolyte (278.0, 295.0, and 310.3 cm^{-1}) arise and can be attributed to the Raman-active vibrations of $AlCl_2Br_2^-$, $Al_2Cl_6Br^-$, and $AlCl_3Br^-$ anions in addition to the Raman peaks for $AlCl_4^-$ and EMI^+ in the EMICl/$AlCl_3$ electrolyte. Meanwhile, due to the total replacement of the bridging Cl atoms with Br atoms within the EMIBr/$AlCl_3$ electrolyte, no Raman modes of the $Al_2Cl_7^-$ anion can be observed (Figure 8G). Consequently, the as-fabricated cell with the EMIBr/$AlCl_3$ electrolyte shows a high initial discharge capacity of 1500 mA h g^{-1} at 251 mA g^{-1} under a much lower polarization. Although much-enhanced capacity than the one using EMICl/$AlCl_3$ electrolyte, the Al–S cell with the EMIBr/$AlCl_3$ electrolyte still shows unsatisfactory cycling performance resulted from the side reactions between the nucleophilic C2 carbon in the imidazole ring of EMI^+ and polysulfide intermediates.

In order to avoid such unwilling interference and make a further improvement in the electrochemical performance of the battery, replacing all EMI^+ cations with N-butyl-N-methylpiperidinium ($NBMP^+$) cations in the ionic liquid electrolyte is adopted. It is well accepted that the dissociation process in different ionic liquid electrolytes has a very important impact on an Al–S battery system. As expected, the battery with NBMPBr/$AlCl_3$ displays the same reaction mechanism with the EMIBr/$AlCl_3$ one. In detail, the $Al_2Cl_6Br^-$ anions in NBMPBr/$AlCl_3$ electrolyte are involved in the dissociation reaction to $AlCl_3Br^-$ and $AlCl_3$ in the cathode discharge reaction and finally to release out Al^{3+} to react with sulfur and form Al_2S_3 (Figure 8H). At the anodic side, $AlCl_3Br^-$ and $AlCl_4^-$ anions are combined with Al^{3+} originating from the elemental Al after losing three electrons to form $Al_2Cl_6Br^-$. Among these multistep electrochemical reactions, step 3 that refers to the Al^{3+} solvation and desolvation takes up the rate-determining factor (Figure 8I), which does significantly affect the kinetic reaction rate due to the high activation energy. That is to say, step 3 would cause a high kinetic barrier when the electron-transfer is fast while the mass-transfer is impeded. Consequently, a 15 times faster reaction rate for the dissociation and the release of free Al^{3+} ions from $Al_2Cl_6Br^-$ anions is reached, as confirmed by exchange current density measurements. Thanks to the optimized reaction kinetics based on the NBMPBr/$AlCl_3$ electrolyte, a reversible Al–S battery with sulfur utilization up to 82% has been achieved. More impressively, the cell delivers a much-enhanced reversible capacity of 400 mA h g^{-1} after 20 cycles, in comparison with the half capacity of the contrast one.

Although Al–S batteries using ionic liquid electrolytes have remarkably given rise to the improvement in aspects of cyclability, capacity, and Columbic efficiency, the high prices of ionic liquids make them hardly be widely used as practical electrolytes in cost control batteries. Many researchers then paid their attention on the exploration of low-cost deep eutectic solvent as electrolyte alternatives with high electrochemical stability and Columbic efficiency, so as to push the development of future practical Al–S energy storage devices while sacrificing part of the ionicity and conductivity. For example, Yu and co-workers[6c] present a low-cost $AlCl_3$/acetamide (AcA) deep eutectic solvent for reversible room-temperature Al–S battery. In this AcA-supported electrolyte system, AcA plays a key role in speeding up the reaction kinetics as it reacts with $AlCl_3$ to generate sufficient $Al_2Cl_7^-$ and $AlCl_4^-$, which is comparable with EMICl/$AlCl_3$ system. As confirmed by density functional theory (DFT) calculations results in **Figure 9**A, there is the definite existence of structural coordination between AcA and cationic Al species. Figure 9A also depicted that the monodentate configurations of $[AlCl_2\cdot(AcA)_2]^+$ are spontaneously exothermic with a negative energy of −6.33 eV, whereas the bidentate structure of $[AlCl_2\cdot(AcA)]^+$ formed by coordination of AcA with $AlCl_2^+$ via both O and N atoms are less stable due to the increased energy. Thus, AcA is more likely to coordinate with $AlCl_2^+$ via O atom to form the monodentate $[AlCl_2\cdot(AcA)_2]^+$. However, $[AlCl_2\cdot(AcA)_2]^+$ is not the dominant reaction agent due to the coexistence of the $Al_2Cl_7^-$ and $[AlCl_2\cdot(AcA)_2]^+$ in the whole electrochemistry procedure. If the dissociation energy barriers of $Al_2Cl_7^-$ and $[AlCl_2\cdot(AcA)_2]^+$ are calculated based on routes (1) and (2) in Figure 9B,C, the corresponding exothermic energies are −1.31 and −1.22 eV, respectively. This means that both dissociation reactions are thermodynamically available. No matter whether it is the final step or the intermediate step, $[AlCl_2\cdot(AcA)_2]^+$ related steps have the higher total reaction energy than that of $Al_2Cl_7^-$, suggesting that the route (2) is less kinetically preferred. Benefiting from the reformed conversion electrochemistry, the as-prepared cell delivers a promising performance, including an initial capacity above 1500 mA h g^{-1}, a capacity retention of 500 mA h g^{-1} for 60 cycles, and a high reversible rate performance (688 mA h g^{-1} at 300 mA cm^{-2}) (Figure 9D). Given the intrinsically nature of chloroaluminate ionic liquids electrolyte, Al-free organic cations may play a role in balancing the electrical neutrality because the conversion electrochemistry in the battery merely involves in the Al-containing anions such as $Al_2Cl_7^-$ and $AlCl_4^-$. By the same token, AcA must coordinate with $AlCl_3$ to form Al-containing cations (in particular $[AlCl_2\cdot(AcA)_2]^+$) to balance the electrical neutrality of the electrolyte. Based on above discussion, the newly AcA supported ionic liquids analog electrolyte provides expected opportunities for optimizing future Al–S battery to attain high-performance and low-cost energy storage systems.

Another type of potential low-cost deep eutectic solvent matching with $AlCl_3$ to allow improved cell cycling stability is the urea supported ionic liquids analog electrolyte.[11b,16] Lin's group[16a] represented a promising Al–S cell with the use of $AlCl_3$/urea electrolyte, different from the usually used imidazolium ionic liquid electrolytes, the urea supported electrolyte shows great potential in improving the cycle stability due to remarkably decreased voltage gap by a promoted discharge voltage plateau around 1.6–2.0 V (Figure 9E). Also, the authors first reveal the

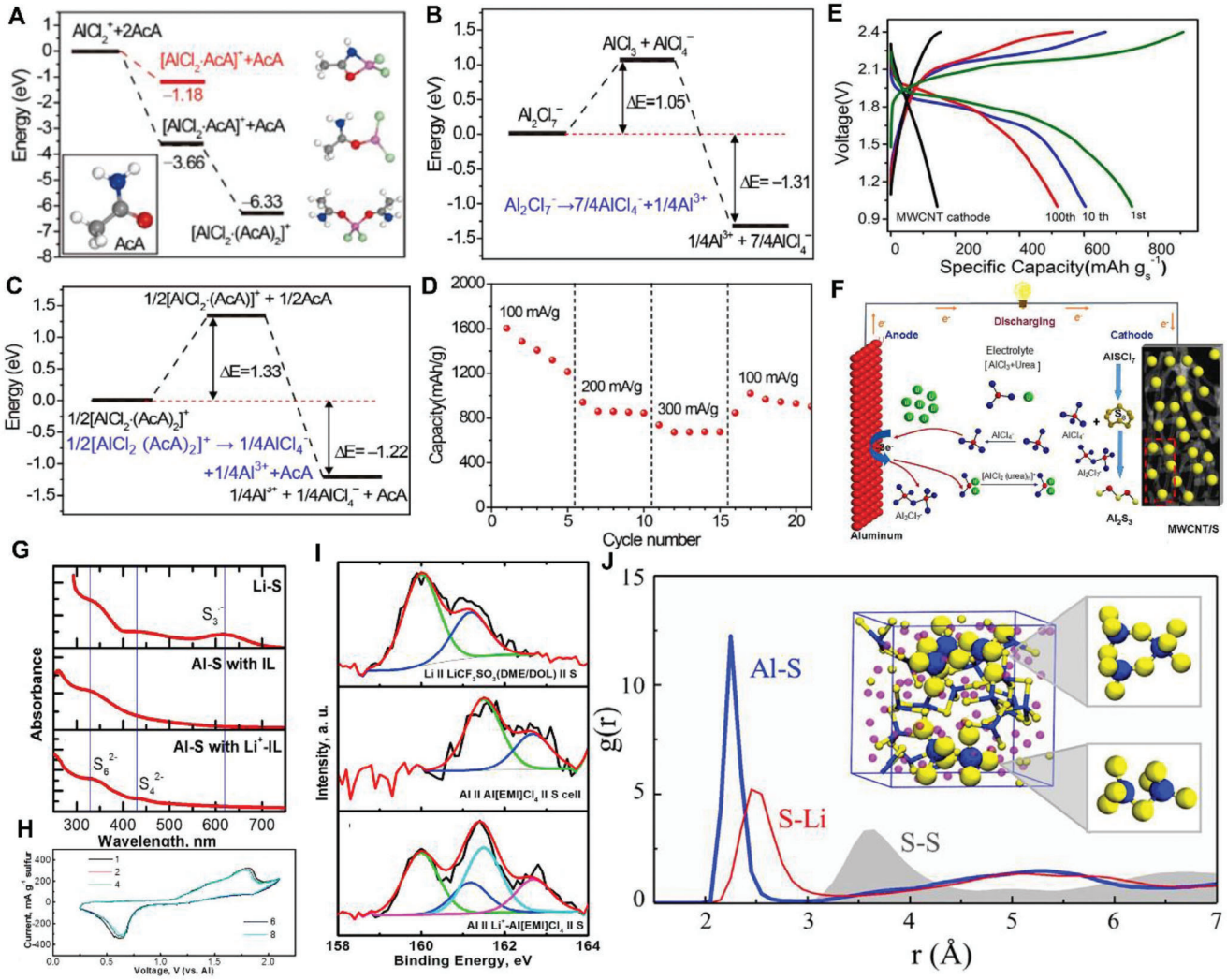

Figure 9. A) Energy profiles of AcA coordinating with $AlCl_2^+$ at different sites (O or N sites). B) Energy profiles of dissociation reactions of $Al_2Cl_7^-$ species and C) the competitive $[AlCl_2{\cdot}(AcA)_2]^+$ configuration. D) Rate performance of the $AlCl_3$/AcA-1.3-based Al–S battery at shifted current density. Reproduced with permission.[6c] Copyright 2019, Elsevier. E) The 10th and 100th charge/discharge capacities of the Al–S cells using the MWCNT/S cathode with $AlCl_3$/urea electrolyte. F) Schematic representation of the urea supported Al–S batteries; Reproduced with permission.[16a] Copyright 2018, Wiley-VCH GmbH. G) UV–vis spectra of the sulfur cathodes discharged to a depth of 350 mA h g^{-1} in the cells with different ionic liquids. H) CV curves of the Al||Li^+–$AlCl_4$||S cell at a scan rate of 0.03 mV s^{-1}. I) High-resolution XPS spectra of S 2p in the deep-discharged sulfur electrodes with different electrolytes. J) Radial distribution functions for Al–S, S–Li, and S–S pairs as predicted from ab initio molecular dynamics (AIMD) simulations. Reproduced with permission.[17b] Copyright 2017, Elsevier.

possible reaction mechanism of this urea-related Al–S battery. As shown in Figure 9F, aluminum foil serves as the anode material coupling with multi-wall carbon nanotubes incorporated sulfur (MWCNT)/S composite as the cathode material. During the discharging process, metallic Al and $AlCl_4$ anions on the anode side are transferred into $[AlCl_2.n(urea)]^+$ cations, sulfur activated by electrons from the external circuit are reduced to polysulfide and further to combine with $AlCl_4$ to form the final Al_2S_3 discharge product. Overall, the urea is essential to play the similar role as the AcA to react with $AlCl_3$ to generate sufficient $Al_2Cl_7^-$ and $AlCl_4^-$ to kinetically ensure the conversion electrothermy. As a result, the cell delivers an initial capacity around 700 mA h g^{-1} at a high current rate of 1000 mA g^{-1} and still sustains a capacity up to ≈500 mA h g s^{-1} after 100 cycles.

So far, despite the remarkable improvement in the battery performance with ionic liquid electrolyte, Al–S batteries still exhibit less reversibility than the Li–S batteries due to the more readily rechargeable Li polysulfide than the other metal polysulfide. This mechanism raises a new possibility that take advantage of the readily rechargeable Li polysulfide or incorporates it into Al polysulfide to form hybrid polysulfide to decrease its energy barrier for redox reactions and making it more electrochemically active, which is quite similar to that in a previous study with respect to the Li^+-ion-activation effect on Mg–S chemistry.[17b,44] In term of this reason, Manthiram and co-workers[17b] established a lithium-ion (Li^+-ion)-mediated hybrid ionic liquid electrolyte with Li salt (LiTFSI or $LiCF_3SO_3$) additives to enable more reversible Al polysulfides. Then, in-depth understanding of

Li^+-ion mediation mechanism is obtained via the combination of a sequence of spectroscopic analyses and DFT calculations in Figure 9G. The specific mediation mechanism can be elaborated from two aspects. Firstly, according to the ultraviolet–visible experimental results, Li^+-ion mediation improves the solubility of S_4^{2-} species, reversing the insoluble nature of S_4^{2-} species formed in the normal ionic liquid electrolyte (Figure 9H). This result supports the differences in the electrochemical characteristics between the Al‖Li^+–$AlCl_4$‖S cell and the Al‖$AlCl_4$‖S cell. To increase the solubility of S_4^{2-} species, the added Li ions reactivate the short-chain Al polysulfides through an ion-exchange reaction to transform them into Al–Li polysulfides or through a strong coordination of Li ions with the surface of Al polysulfides to form Al–Li polysulfides. Accordingly, the electrochemical kinetic barriers for the redox reactions of Al polysulfides are therefore reduced (Figure 9H). Moreover, other important mediation mechanism influencing the battery performance involving in the formation of final discharge product of Li_3AlS_3 is further confirmed by XPS analysis (Figure 9I). In term of the S 2p XPS spectra of the sulfur/Ti electrodes taken from the three discharged cells, the Al‖Li^+–$Al^{[45]}Cl_4$‖S cell shows characteristics of a mixture of Li_2S- and Al_2S_3-like structures. The corresponding deconvoluted curves suggest that the ratio of sulfur assigning to the Li_2S- and Al_2S_3-like species is approximately 1:1, implying that the discharge product is most likely in a stoichiometric form of $3Li_2S{\cdot}Al_2S_3$ (Li_3AlS_3). Upon inspection of the structure of the simulated Li_3AlS_3 (Figure 9J), anionic Al–S clusters are stabilized by Li^+ cations because the Al atoms tend to be surrounded by four or five S atoms forming isolated or somewhat extended Al–S complexes where the S atoms are either terminal (bonded to one Al atom) or bridging (bonded to two Al atoms). Though these comprehensive analyses, the final discharge product of the Li^+-ion-mediated cell is finally discerned as Li_3AlS_3-like species. The coordination of Li to S minimizes the formation of Al═S double bonds upon fully discharged and thus promotes reactivation of sulfide species during charge, which hence significantly improves the reversibility of room-temperature Al–S chemistry. However, it is still a long way to go to realize a practical battery technology with hybrid electrolytes in the future.

Not limited to the widely accepted Al–S configurations, anions with strong oxidizing ability in an ion liquid electrolyte can oxidize sulfur in a highly reversible manner through manipulating the voltage window. Based on the voltage-dependent feature of the $AlCl_3$/carbamide ionic liquid reported by Lin et al.,[16a] Qiao's group[17a] successfully demonstrated the reversible sulfur oxidation process in this electrolyte system, where sulfur is electrochemically oxidized by $AlCl_4^-$ to form $AlSCl_7$. Such sulfur oxidation is: 1) highly reversible with an efficiency of ≈94%; and 2) workable within a wide range of high potentials, allowing the Al–S battery based on this sulfur oxidation can be cycled steadily. The sulfur oxidation and reduction-based Al–S electrochemistry pathways are schematically summarized in **Figure 10**A. The $AlCl_4^-$ and $Al_2Cl_7^-$ anions serve as the oxidizing and reducing agents to react with sulfur, respectively. As a matter of fact, the two products are observed on the scanning transmission electron microscopic (STEM) images after charging to 2.4 V and discharging to 0.2 V. After fully charging, a periodic layered structure with (100), (102), and (306—) planes is recorded in the Fast Fourier Transform (FFT) patterns in Figure 10B. The observation of (102) plane corresponds well with the in situ XRD patterns. The ordered atom distribution can be clearly identified due to that Al, S, and Cl atoms are orderly arranged, coinciding well with designed and simulated $AlSCl_7$ images from [010] observation. By comparison, the crystallized structure of the reduction product at 0.2 V is well matched with Al_2S_3.

Then, the synchrotron-based near-edge X-ray absorption fine structure (NEXAFS) spectra are combined with X-ray photoelectron spectra (XPS) and in situ Raman spectra to track the reaction intermediates during the sulfur oxidation process. As shown in the S K-edge NEXAFS spectra (Figure 10C), the shifted peak position (≈2472 eV) of oxidation products from 2.2 to 2.4 V is nicely located between the peaks of 0-valence and +6-valence sulfur as compared to the reference samples of elemental sulfur, $N_2S_2O_3$, and Li_2SO_4, suggesting the efficient oxidation of sulfur to higher valence at high voltages. The positive shift of Cl characteristic peak is also identified from the Cl L-edge spectra at ≈201.3 eV (Figure 10D), which is attributed to the formation of S–Cl bonds in $AlSCl_7$. To quantify the sulfur valence during its oxidation, the XPS measurements at different oxidation voltages are carried out. In the S 2p XPS spectra (Figure 10E), the peaks located at ≈169.4 and ≈168.3 eV between the +2 thiosulfate and +6 sulfate gradually appear, which are assigned to the +4 sulfur, confirming the stable presence of $AlSCl_7$ oxidized products. During the charging process, the intensity of the Raman peaks (≈145, ≈210, and ≈462 cm^{-1}) assigned to sulfur gradually weakens, indicating the conversion from sulfur to $AlSCl_7$ (Figure 10F). And these Raman peaks reappear in the reverse process, which is the strong evidence of the high reversibility of sulfur oxidation. Notably, a new emergence of peak located at 530 cm^{-1} (Figure 10G) should be attributed to the vibration of SCl_3^+ cations that are soluble in the electrolyte. Therefore, $AlSCl_7$ tends to decompose to $AlCl_4^-$ and SCl_3^+ intermediates, leading to the loss of sulfur during electrochemical cycling. These results well characterize the phase evolution for the oxidation and reduction process of sulfur, where $AlSCl_7$ is the main products. The Al–S battery worked on sulfur oxidation process can run steadily over 200 cycles with an average voltage plateau around 1.8 V, which is the highest operation voltage for Al–S batteries, showing a great advantage of the sulfur oxidation pathway for the design of viable high-voltage Al–S batteries.

4. Reversible High-Efficient Aluminum Anodes

In order to fulfill the requirement of the long service life of Al–S systems for large-scale energy storage applications, the anodic aluminum is also of remarkable significance to be protected and modulated for a lot of rechargeable cycles. Typically, the long-term cycling stability of an Al–S battery is highly associated with its redox reactions, i.e., plating and stripping behavior on the Al anode, which has significant influences in the overall battery electrochemical performance. The electrochemical reaction of Al metal anode in Al–S batteries is basically similar to other ILs-based AIBs, which can be explained through the following equation: $Al + 7AlCl_4^- \rightarrow 4Al_2Cl_7^- + 3e^-$, corresponding to the stripping of Al metal. The above equation clearly described that the ideal stripping in the Al anode plating/stripping process involves the complete dissolution of Al metal into the electrolyte,

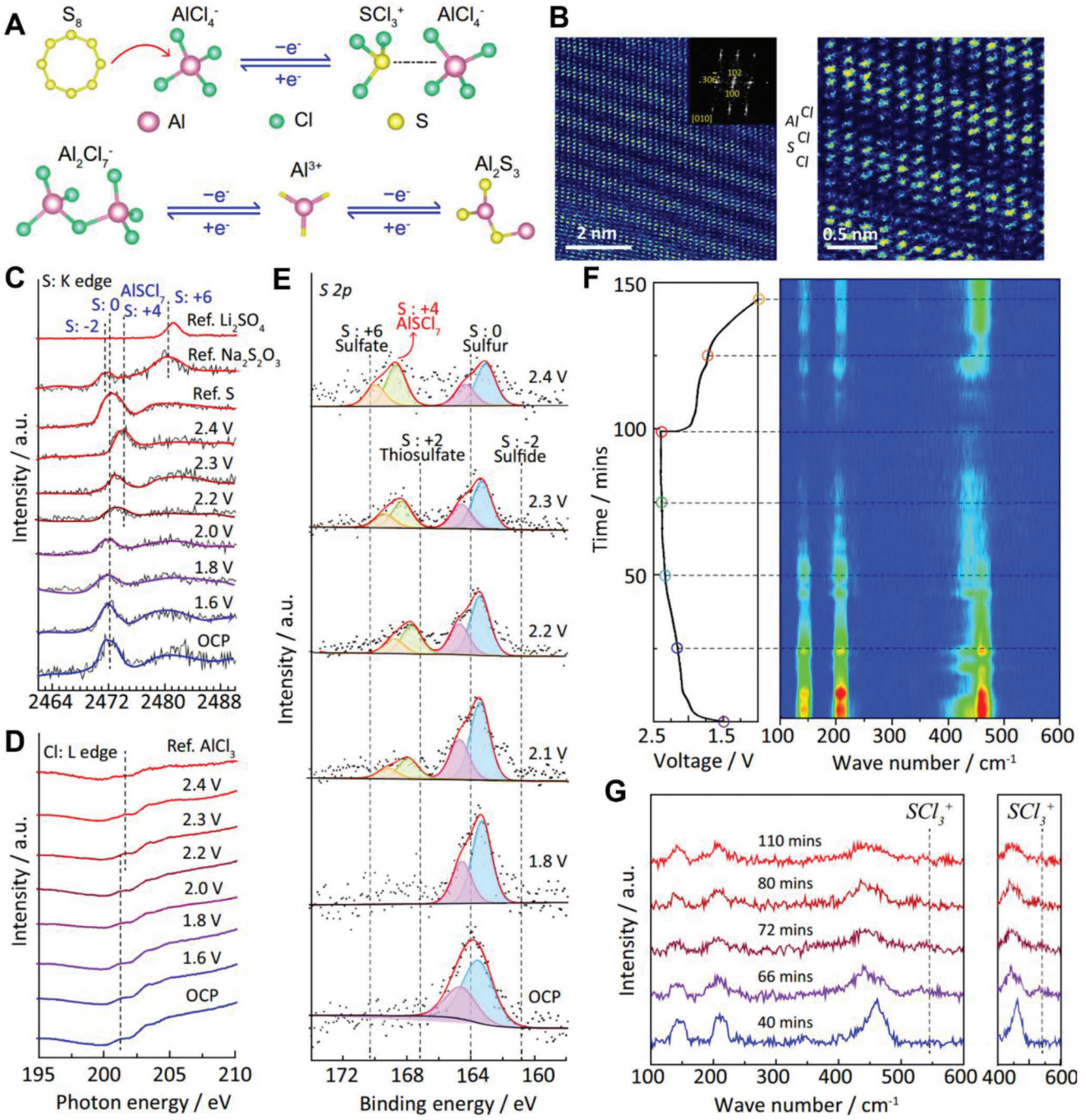

Figure 10. A) Schematics for sulfur oxidation and sulfur reduction processes with $AlCl_4^-$ and $Al_2Cl_7^-$ anions, respectively. B) High-resolution TEM images of $AlSCl_7$ and the simulated microscopic image of $AlSCl_7$ observed from [010] direction; Ex situ NEXAFS spectra of S/CNT cathode with different voltages recorded at the C) S K-edge and D) Cl L-edge. E) Ex situ S 2p XPS spectra of S/CNT cathode at different oxidation voltages. F) The charge–discharge curves of Al–S batteries at 0.2 A g^{-1} and their real-time Raman contour map for S/CNT cathode. G) Raman spectra at different times extracted from the contour pattern in (F). Reproduced under the terms of the Creative Common CC BY license.[17a] Copyright 2021, The Authors, published by Springer Nature.

in which undesirable reactions are likely to occur during Al electrodeposition to affect Al metal stripping efficiency. This phenomenon would bring about incomplete Al metal dissolution, and hence causes uneven growth of Al on the anode surface to form dendrite growth and eventually bring about batteries' failure.

4.1. Protection Layer Preventing Aluminum Disintegration

So far, the researches about Al metal anode in Al–S battery have not been focused on yet. Motivated by the Al metal protection of AIBs, employing protection layer on the anodic Al surface is a potential strategy to modulate the plating and stripping path of Al electrochemistry for high-capacity retentions.[40] For instance, Gao and co-workers[14a] discover that aluminum oxide film can efficiently restrict the growth of crystalline Al dendrite and thus improves the cycling stability of Al anode. The key role of the surficial aluminum oxide film in protecting the Al metal anode lies in decreasing the nucleation sites, controlling the metallic dendrite growth, and preventing the electrode disintegration. As revealed in **Figure 11**A, the defect sites in aluminum oxide film provide channels for infiltration of the 1-ethyl-3-methylimidazolium chloride-based ionic liquid electrolyte ($AlCl_3$/[EMIm]Cl) and benefit further stripping/depositing. However, this protection and modulation strategy in Al-based batteries are still at an infant stage in comparison to Li/Na-based batteries, due to the uncontrollable corrosion and depletion of the protection layer by the corrosive chloroaluminate. Lee et al.[14b] proposed a locally selective attacking on the Al metal surface by chloroaluminate anions to continuously expose the active Al to the electrolyte directly. XRD patterns in Figure 11B show the evolution of the crystallinity of the Al metal surface dipping in electrolyte. As the dipping time progress, new lattice planes (111), (220), and (311) at 38.5°, 65.1°, and 78.2° for Al metal are observed owing to the erosion effect of chloroaluminate anions. High-resolution Al 2p spectra in Figure 11C further confirm the gradual intensity increase of the oxide peak while the Al metal peak becomes relatively weak, suggesting the reconstruction of the aluminum oxide layer by the dissolution and deposition of Al ions owing to galvanic corrosion. After dipping, the Al surface undergoes unavoidable dissolution to deepen cracks due to the penetration and corrosion of the acidic ionic liquid electrolyte (ILE), generating island oxide films and craterlike morphology on the dissolved Al surface (Figure 11D,E). Based on this series of analyses, the instability mechanism of the Al anode is summarized in Figure 11F. The metallic Al surface covered with thin oxide film is preferentially attacked and dissolved by acidic chloroaluminate anions, such as $AlCl_4^-$, $Al_2Cl_7^-$, and Cl^-. Thereafter, the dissolved Al ions are recombined with oxygen species, followed by deposition of a newly formed Al_2O_3 on the defective sites of the Al metal surface. The Al^{3+} transfer and the Al deposition are guided to avoid the continuous growth of Al dendrite during this repeated film removal and regrowth process. In virtue of this side effect of corrosion, constructing porous protection layer to modulate the Al electrochemistry is a wise strategy to stable the battery performance. Wu and co-workers[14c] put forward an interfacial regulation strategy resorting to corrosive $AlCl^{3-}$ based electrolyte to etch the protected Al_2O_3 film on the Al anode surface, thus tunneling suitable accesses for Al^{3+}, as illustrated in Figure 11G. Then, coupling this pretreated anode with the noncorrosive aluminum trifluoromethane sulfonate ($Al(OTF)^{3-}$) based electrolyte is workable to get stable Al/electrolyte interface and dredge Al^{3+} transformation passages to improve the cycling performance of the rechargeable aluminum batteries. Although the protected Al_2O_3 film can resist the Al anode from unexpected corrosion and interference from the electrolyte, Al^{3+} deposition/dissolution process is blocked by the dense Al_2O_3 film, while after partial removal of the Al_2O_3 film, the reaction proceeds smoothly. Furthermore, the SEM images of Al foil after immersed in 0.5 mol L^{-1} $Al(OTF)_3$/[BMIM]OTF and $AlCl_3$/[BMIM]Cl=1.1:1 ionic liquid are also shown in Figure 11H, respectively. By comparison with the initial Al foil, no change is found on Al foil immersed in $Al(OTF)_3$/[BMIM]–OTF ionic liquid, whereas pitting corrosion occurs on Al foil immersed in $AlCl_3$/[BMIM]Cl = 1.1:1 ionic liquid. Given an overall consideration of the electrochemical behavior with the treated morphology, it is found that electrochemical reaction can merely happen on the Al anode surface with $AlCl_3$/[BMIM]Cl pretreatment, by which the dense oxide film is etched and the fresh Al surface is exposed. As an obvious contrast, a blank rechargeable aluminum battery using Al–$(OTF)_3$/[BMIM]OTF ionic liquid electrolyte with intact film Al anode exhibits electrochemical inertness.

4.2. Kinetical Guidance of the Al^{3+} Flux against Dendrite Growth

It is obvious that these researches disseminate the key impact of the interface between the anodic Al and the electrolyte on the electrochemical activity of the battery regardless of the immature nanotechnology and mechanism, giving an effective reference to the design and guiding the development of the anodic interfaces in Al–S battery systems. Regarding the in-depth understanding, the future investigation of the interfacial effect on aluminum anode can resort to the more extensive studied anodic Li/Na.[3g,22b,46] Upon the Al–S electrochemistry, the anodic Al process is well accepted as a stepwise Al plating/dissolution from Al ion/atom desolvation, to nucleation and diffusion. Both in the aqueous electrolyte and in the ILE, the fast step of releasing free Al^{3+} from the solvated cluster is responsible for the uniformity of ionic flux. As a result, similar to Li metal plating, to obtain the Al ion/atom, the high barriers of desolvation, nucleation, and diffusion must be overcome for uniform and lateral deposition, which are the main causes of the random plating and dendrite growth that make battery failure.[19a] Without altering the Al electrochemistry, shortening the ion diffusion pathway and averaging ion flux is a feasible way to regulate the Al plating behaviors. Alloys, with the intrinsic ability to uniformize ion flux and guide the ion transport, can be applied as modulators against Al dendrite growth.[47] Jiang's group report that aluminum–copper alloy lamellar heterostructures are used as anode active materials to achieve dendrite-free Al deposition during stripping/plating cycles in aqueous electrolyte.[22a] Eutectic $Al_{82}Cu_{18}$ (at%) alloy (E-$Al_{82}Cu_{18}$) with a lamellar nanostructure consisting of alternating α-Al and intermetallic Al_2Cu nano lamellas is synthesized through eutectic reaction (**Figure 12**A). The optical micrograph of E-$Al_{82}Cu_{18}$ alloy sheets further confirms that the eutectic solidification produces an ordered lamellar nanostructure of

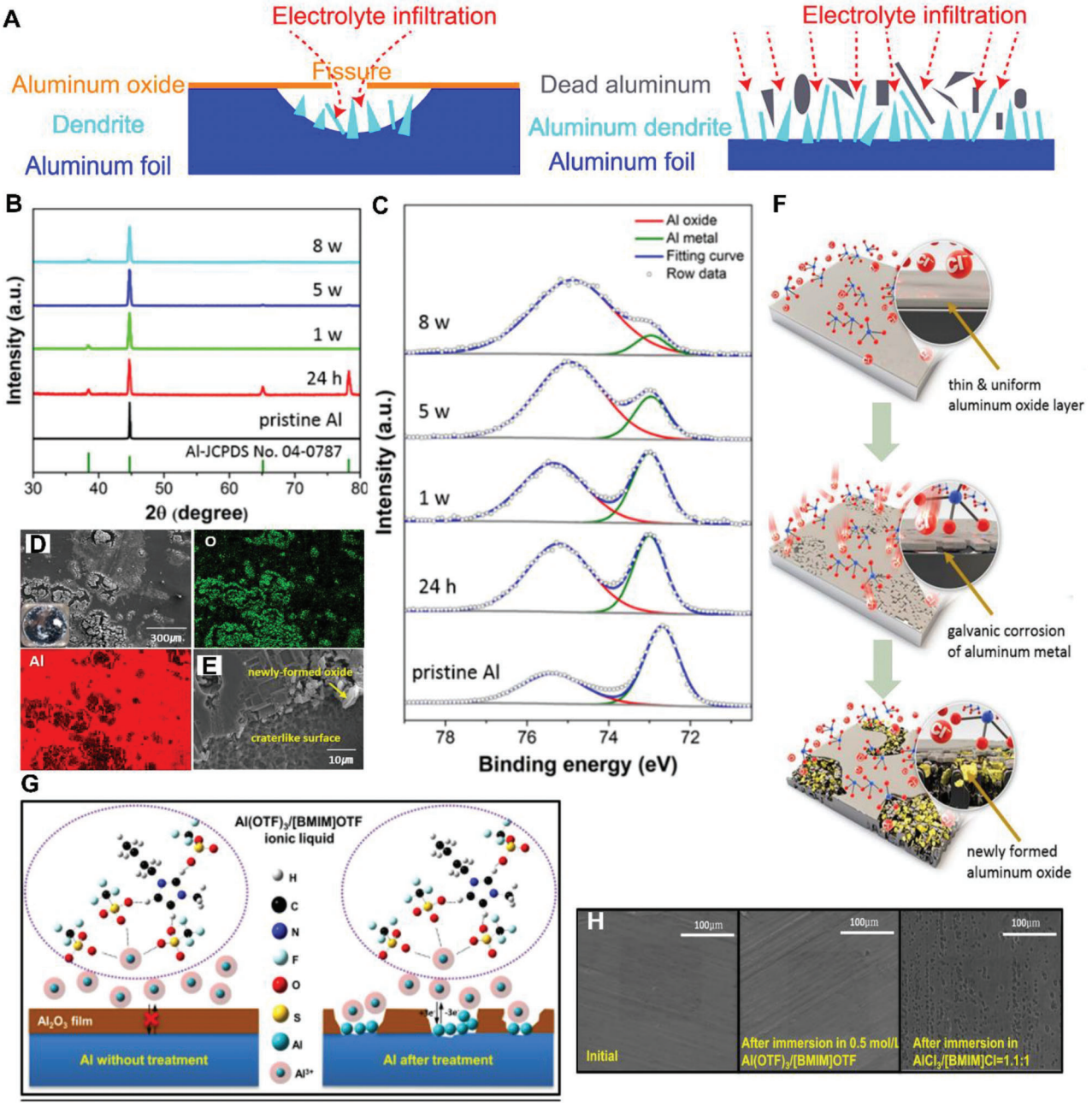

Figure 11. A) Schematic models of cycled Al metal with and without surface oxidation layer. Reproduced with permission.[14a] Copyright 2017, American Chemical Society. B) XRD patterns and C) high-resolution XPS spectra of Al 2p collected on the Al metal dipped in ionic liquid over time. D,E) SEM images and EDS mapping of Al and O obtained on Al metal dipped in electrolyte after 8 weeks. F) Schematic illustration of morphology changes on the Al metal surface induced by galvanic corrosion and oxidation processes in acidic ionic liquid electrolyte; Reproduced with permission.[14b] Copyright 2018, Institute of Physics. G) Schematic diagram of Al deposition/dissolution on surface of untreated and treated Al anode. SEM images of Al foils H) before and after immersion in different liquids for 24 h. Reproduced with permission[14c] Copyright 2016, American Chemical Society.

alternating α-Al and intermetallic Al_2Cu lamellas with thicknesses of ≈150 nm and ≈270 nm under the lamellar spacing of ≈420 nm (Figure 12B). This microstructure is also illustrated by scanning electron microscope (SEM) backscattered electron images and its corresponding energy dispersive spectroscopy (EDS) elemental mappings in Figure 12C. In order to recognize the specific roles of α-Al and Al_2Cu nano lamellas in the E-$Al_{82}Cu_{18}$ electrodes, ex situ SEM-EDS elemental mapping is carried out after deep Al stripping and plating at 1 mA cm^{-2} for 10 h. During this process, the Al_2Cu is arranged to form a lamella-nanostructured 2D pattern and the electrodeposited Al atoms are uniformly distributed in the channels to be sandwiched

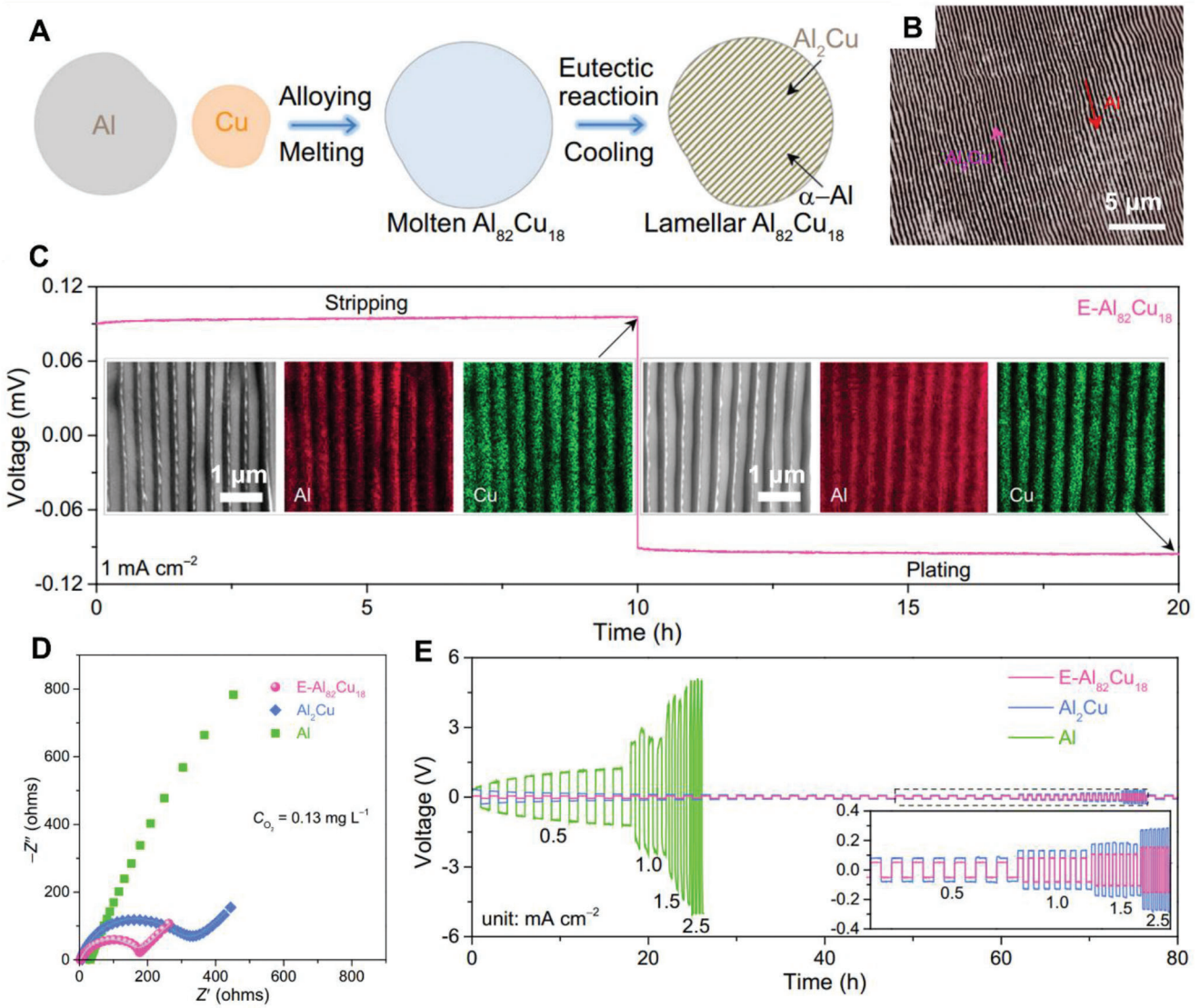

Figure 12. A) Description of the procedure to prepare lamella nanostructured E-$Al_{82}Cu_{18}$ alloy and B) the corresponding optical micrograph. C) Typical stripping/plating voltage profile (pink line) of E-$Al_{82}Cu_{18}$ symmetric cells in 2 M $Al(OTF)_3$ aqueous electrolyte. Insets: representative ex-SEM images and the corresponding SEM-EDS elemental mappings of Al and Cu for the E-$Al_{82}Cu_{18}$ electrode after Al stripping/plating. D) EIS spectra of as assembled E-$Al_{82}Cu_{18}$, Al_2Cu, and pure Al symmetric cells in 2 M $Al(OTF)_3$ aqueous electrolyte. E) Comparison of rate performance for symmetric cells based on the three electrodes at various current densities. Reproduced under the terms of the Creative Common CC BY license.[22a] Copyright 2022, The Authors, published by Springer Nature.

between the Al_2Cu lamellas. Triggered by such periodical Al/Al_2Cu galvanic couples, the E-$Al_{82}Cu_{18}$ electrode decreases the charge transfer resistance (R_{CT}) to as low as ≈160 Ω, more than 20-fold lower than ≈3880 Ω of the monometallic Al with a thicker passivating oxide layer (Figure 12D). In short, the Al_2Cu lamellas serve as electron transfer pathway to facilitate Al stripping from the constituent Al lamellas and work as modulators to guide subsequent Al plating against dendrite formation, enabling improved Al reversibility at low potentials. Benefiting from this, the symmetric E-$Al_{82}Cu_{18}$ cell exhibits an obviously decreased hysteresis when the current density is increased from 0.5 to 2.5 mA cm^{-2} (Figure 12E), suggesting the acceleration of the reaction kinetics and the fast plating/stripping behavior of Al atom in the aqueous $Al(OTF)_3$ electrolyte. Inspired by this alloy strategy, the generation and growth of aluminum dendrite are mainly attributed to the random aluminum ion behaviors in nucleation and the sluggish surface atom diffusion. Therefore, it is a simpler and more straightforward approach to electrochemically regulate the Al ion/atom diffusion kinetics to prevent the random aluminum ion/atom behaviors. For pursuing higher energy density, if the size of alloy or metal is lowered to atomic level, the capability of activity is the highest and reaches the maximum of 100%. Learning from the modulation of Li ion/atom kinetics, the single-atom catalysts (SACs) are expected to be introduced into aluminum anodes to decrease the barriers from desolvation, atom nucleation to atom diffusion.[2h,3d,23b,40,48] For example, our

team[46c] put forward an artificial protective layer to modulate the interfacial surface on Li metal in virtue of the highly active single metal atom anchored in a vacant catalyst growing on the hierarchical porous nanocarbon (SACo/ADFS@HPSC), and the corresponding kinetically mechanism for guiding the deposition of metallic lithium is proposed. In comparison to the random distribution of plated metallic lithium on the pristine Li surface, the numerous lithophilic sites from the active single atoms are advantageous for attracting and allocating the initial lithium ions for subsequently homogeneous plating. Thereafter, the fresh lithium tends to deposit along the uniform nucleated Li position without growing any dendrite, regulating the Li electrochemistry, and prolonging the lifespan significantly, whereas the random plated lithium on the pristine Li surface attracts more causal lithium to grow undesirable dendrites. In the subsequent investigation,[46d] we further confirmed and depicted the SACs as kinetic activators in propelling the surface spreading and lateral redistribution. In this regard, we simulate the diffusion kinetics and plating behaviors of lithium atoms with single atomic catalysts through density functional theory (DFT). Upon introducing the active SACs, the lithiophilicity energy is significantly enhanced from 1.388 to 1.611 eV, implying that the Li atom behaviors are influenced by SACs. More importantly, the high forming energy barriers (0.42 and 0.44 eV) and the low breaking energies (0.09 and 0.12 eV) of the lithium dimer demonstrate that the SACs help lithium atoms to diffuse in plane against local aggregation and dendrite growth. Our creative works help to open a future direction of using the catalytic materials to manipulate electrochemical behaviors for uniform stripping/plating Al surface.[46c,d,49]

5. Conclusion and Prospects

In summary, the electrochemistry of high energy density Al–S battery has been brought into focus from sulfur cathode conductive constructions for polysulfides inhibition and electrolyte exploitation or modification to achieve high ion transfer or resist the occurrence of undesirable dendrite formation in the anode. Despite several achieved progresses in recent years, the challenges such as sluggish conversion kinetics, and electrolyte compatibility are still remained, resulting in the inferior cycling stability and severe potential hysteresis. Aiming at eliminating the limitations in the Al–S battery, the progresses of sulfur cathode are first summarized from the aspect of conductivity to adsorption and finally to catalytic capability properties to break off the electrochemical barriers in promoting the conversion kinetics. Then, the categories of aqueous and organic electrolytes are comprehensively reviewed to achieve high ion transport and positive mediation of the anodic Al stripping/plating including alloy incorporation, protection, and anti-corrosion layers. At the same time, the following aspects to further improve Al–S development should be paid more attention.

5.1. Developing High Areal Loading Sulfur Cathode at High Current Rate for Practical Applications

The current researches of sulfur cathode design in Al–S systems are still infantile. In this regard, the future development of the S composite cathode materials can be directed, including: 1) Designing a conductivity-enhanced matrix to accommodate insulative sulfur; 2) Chemically heteroatom doping to enhance adsorbed ability of bonding polysulfides at the premise of physically confining sulfur within the porous structure; 3) Incorporating electrocatalysts to promote the multistep S related interconversion kinetics. Although the similar phenomena of polysulfide shuttling and insulative nature of sulfur/Al_2S_3 existed in the cathode, a new fresh viewpoint should be taken since the reaction pathway is strictly different. For better investigations, the deep insight into catalytic mechanisms with operando characterizations should also be paid more attention. From a practical point of view, improving the mass loading of the sulfur cathode is the most likely pathway to get high areal capacity to satisfy the commercial demand. Unfortunately, the high mass loading cathodes is bound to face more serious issue of polysulfide shuttling, bringing about failure in some proposed strategies. Therefore, it is essential to take effective steps to improve sulfur loading of the cathode and optimize the electrochemical performance with low E/S ratio. To realize the goal of high energy density, a viable trial is to propose large-area pouch cell with lean electrolyte. On the premise of high sulfur loading, the fast-charge technology and long lifespan should also be paid more attention due to the fast-charge and long durance consumption demand in our daily life. The intrinsic conductivity and the conversion kinetics are the decisive factors to the fast-charge and high-loading batteries. In light of this fact, using highly conductive host incorporated high-efficiency kinetic promoters, such as carbon networks supported active SACs, can provide more potential than common adsorption and catalytic materials.

5.2. Introducing Catalytic Strategy to Modulate the Al Diffusion Kinetics against Dendrite Growth

Currently, the strategies including protection layer and using alloy to uniformize the Al^{3+} fluxes had been employed to prevent the Al corrosion in Al metal batteries. Simply relying on this protection and guiding strategy, the insufficient active site numbers and sluggish ion kinetics would confront uncontrolled Al dendrites formation under Al plating, resulting in low Al utilization and high safety hazards. According to previous studies on Li electrochemistry, the catalytic layer on the anodic side may also have the potential to manipulate electrochemical behaviors for uniform Al stripping/plating through kinetically modulating interfacial Al ion/atom diffusion behaviors for lateral deposition without any dendrite growth. Therefore, constructing active catalysts such as defect-rich catalysts (DRCs) and single atomic catalysts (SACs) is expected to significantly improve the performance of Al–S batteries.

5.3. Developing New Support Materials to Synthesize High Concentration SACs

As discussed above, transferring the routine catalytic methods to SACs strategy is more likely to remit shuttle effect through boosting the phase conversion kinetics of sulfur species and regulating the Al^{3+} diffusion kinetics at the expense of sacrificing little

energy density, which disseminates great potential to comprehensively solve the key issues the Al–S batteries faced. So far, carbon materials, primarily N-doped carbons, are often used as carriers for single atoms. Unfortunately, within this type of supporter model, one metallic atom is often stabilized by four heteroatoms ($M\text{-}N_4$) as a coordination structure, exposing great restriction of the diversity of active sites and limitation of low metal concentration. On account of the significant impact of the coordination environment and the geometric structure of the ligand site on the concentration and activity of SACs, more efforts are expected to develop new support materials with affluent anchoring sites and controllable coordination numbers. In this regard, future investigations should be devoted to the exploitation of various kinds of defective metal-based compounds that are rich in coordination structures and electron structures are adjustable, which is right for constructing high-concentration SACs with strong activity for high-performance Al–S batteries.

5.4. Looking for and Synthesizing Compatible Electrolytes with the Sulfur Cathode and Al Anode for High Kinetical Electrochemistry

As we all know that the electrochemical activity of Al–S batteries in the $AlCl_3$–NaCl melts electrolyte is strongly dependent on the high-temperature surroundings, which greatly restricts the adaptability in room temperature demand. The aqueous electrolytes enable Al metal to realize partially reversible plating and stripping at room temperature, however, the large voltage hysteresis and long-time instability are still waiting for being addressed. Also, its compatibility to redox sulfur should also be aroused. The room-temperature ionic liquid system with desirable properties of higher ionic conductivity exhibited corrosion to Al anode, inevitably shortening the lifespan. Ideally, the electrolyte systems should have merits in: wide working voltage window; high electrochemical stability; high transportation of Al ion or related Al-based species; no corrosion to battery electrodes or components; all-climate suitability. Thereby, it is urgent to explore more optimal electrolytes to couple well with both the sulfur cathode and anodic Al to fully resolve the remained issues in each kind of electrolytes. More importantly, the carrier in current workable electrolyte is $AlCl_4^-$ or $Al_2Cl_7^-$ species, however, it migrates slowly in the electrolyte and needs to convert to bare Al^{3+} ions in the interface. In this regard, similar to Li electrolyte, to develop the simple Al^{3+} ion-based electrolyte is the most promising one.

5.5. Extracting the Working Principles from Simulations to In Situ Characterizations

Up to date, the practical working principles and the intermediate molecules in the Al–S batteries are still undecided. In situ characterizations (such as Raman, XRD, and XAS) are potential to be introduced into this field to trace the evolution of the sulfur and aluminum related species to uncover the detailed behaviors of the battery system with suitable electrolyte. On the other hand, it is necessary to investigate the real catalytic centers via in situ techniques if electrocatalysts are incorporated into the electrodes for higher kinetical performance. For instance, the visual in situ transmission electron microscopy (TEM) together with electron energy loss spectroscopy (EELS) could record the real-time morphology changes upon catalyzing sulfur species. Using the in situ Raman or XAS spectroscopy may help to observe the evolution process of sulfur or catalyst centers. Meanwhile, the dynamic information would greatly contribute to construct the simulating model for obtaining more accurate theoretical calculation such as binding energy, diffusion energy, and Gibb's free energy for each reaction steps etc., further paving the access for the deep understanding of the reaction mechanism of Al–S batteries. At the same time, theoretical simulation is a beneficial tool to significantly simplify the experimental steps and save the experimental cost.

Acknowledgements

The authors acknowledge financial support from the National Key R&D Program of China (2021YFA1201503), the Natural Science Foundation of Jiangsu Province (BK 20210130), National Natural Science Foundation of China (No. 5217191, 22279161,21972164, 22078136, 21773294, 11734013), the ISF-SFC joint research program (No. 51961145305 (NSFC), Shaanxi Key Program for International Science and Technology Cooperation Projects (No. 2021KWZ-12), Shaanxi Natural Science Basic Research Plan (No.2022JQ-137), Innovation and Entrepreneurial Doctor in JiangSu Province (JSSCBS20211428), Scientific Research Program-Shaanxi Provincial Education Department (20JS104) and China Postdoctoral Science Fundation (2023M732561, 2023M731084). J.W. thanks the scholarship support provided by the Alexander von Humboldt Foundation. The authors thank the technic support from Nano-X, Suzhou Institute of Nanotech and Nano-bionics, Chinese Academy of Sciences. J. Z. and C. Y. is also grateful to the support by the Youth Innovation Team of Shaanxi Universities.

Conflict of Interest

The authors declare no conflict of interest.

Keywords

Al electrodeposition, aluminum–sulfur batteries, electrochemical mechanisms, ionic liquid electrolytes, stable rechargeability, sulfur cathodes

Received: May 22, 2023
Revised: June 25, 2023
Published online: July 14, 2023

[1] a) G. A. Elia, K. Marquardt, K. Hoeppner, S. Fantini, R. Lin, E. Knipping, W. Peters, J. F. Drillet, S. Passerini, R. Hahn, *Adv. Mater.* **2016**, *28*, 7564; b) D. Gelman, B. Shvartsev, Y. Ein-Eli, *J. Mater. Chem. A* **2014**, *2*, 20237; c) X. Fu, G. Jiang, G. Wen, R. Gao, S. Li, M. Li, J. Zhu, Y. Zheng, Z. Li, Y. Hu, L. Yang, Z. Bai, A. Yu, Z. Chen, *Appl. Catal., B* **2021**, *293*, 120176; d) Z. Han, S. Zhao, J. Xiao, X. Zhong, J. Sheng, W. Lv, Q. Zhang, G. Zhou, H. M. Cheng, *Adv. Mater.* **2021**, *33*, 2105947; e) J. Wang, L. Jia, S. Duan, H. Liu, Q. Xiao, T. Li, H. Fan, K. Feng, J. Yang, Q. Wang, M. Liu, J. Zhong, W. Duan, H. Lin, Y. Zhang, *Energy Storage Mater.* **2020**, *28*, 375; f) J. Wang, W. Qiu, G. Li, J. Liu, D. Luo, Y. Zhang, Y. Zhao, G. Zhou, L. Shui, X. Wang, Z. Chen, *Energy Storage Mater.* **2022**, *46*, 269.

[2] a) M. Guo, X. Zhang, T. Yang, Q. Dang, X. Li, Y. Wang, G. Zhang, *J. Power Sources* **2020**, *456*, 227933; b) N. Jayaprakash, S. K. Das, L. A. Archer, *Chem. Commun.* **2011**, *47*, 12610; c) M. Jiang, C. Fu, R. Cheng, T. Liu, M. Guo, P. Meng, J. Zhang, B. Sun, *Chem. Eng. J.* **2021**, *404*, 127124; d) M. Jiang, J. Yang, J. Ju, W. Zhang, L. He, J. Zhang, C. Fu, B. Sun, *Energy Storage Mater.* **2020**, *27*, 96; e) S. Kumar, R. Satish, V. Verma, H. Ren, P. Kidkhunthod, W. Manalastas, M. Srinivasan, *J. Power Sources* **2019**, *426*, 151; f) Z. Liang, J. Shen, X. Xu, F. Li, J. Liu, B. Yuan, Y. Yu, M. Zhu, *Adv. Mater.* **2022**, *34*, 2200102; g) X. Zheng, T. Ahmad, W. Chen, *Energy Storage Mater.* **2021**, *39*, 365; h) H. Shi, X. Ren, J. Lu, C. Dong, J. Liu, Q. Yang, J. Chen, Z. S. Wu, *Adv. Energy Mater.* **2020**, *10*, 2002271; i) G. Liu, W. Wang, P. Zeng, C. Yuan, L. Wang, H. Li, H. Zhang, X. Sun, K. Dai, J. Mao, X. Li, L. Zhang, *Nano Lett.* **2022**, *22*, 6366.

[3] a) H. Lin, Z. Zhang, Y. Wang, X. L. Zhang, Z. Tie, Z. Jin, *Adv. Funct. Mater.* **2021**, *31*, 2102735; b) S. F. Liu, X. L. Wang, D. Xie, X. H. Xia, C. D. Gu, J. B. Wu, J. P. Tu, *J. Alloys Compd.* **2018**, *730*, 135; c) Q. Song, H. Yan, K. Liu, K. Xie, W. Li, W. Gai, G. Chen, H. Li, C. Shen, Q. Fu, S. Zhang, L. Zhang, B. Wei, *Adv. Energy Mater.* **2018**, *8*, 1800564; d) J. Wang, H. Hu, S. Duan, Q. Xiao, J. Zhang, H. Liu, Q. Kang, L. Jia, J. Yang, W. Xu, H. Fei, S. Cheng, L. Li, M. Liu, H. Lin, Y. Zhang, *Adv. Funct. Mater.* **2022**, *32*, 2110468; e) J. Wang, J. Zhang, S. Duan, T. Li, L. Jia, H. Liu, L. Li, S. Cheng, H. Hu, M. Huang, H. Hu, S. Zhang, Q. Xiao, H. Lin, *Chem. Eng. J.* **2022**, *429*, 132352; f) Q. Wu, Z. Yao, A. Du, H. Wu, M. Huang, J. Xu, F. Cao, C. Li, *J. Mater. Chem. A* **2021**, *9*, 5606; g) J. Wang, J. Yang, Q. Xiao, J. Zhang, T. Li, L. Jia, Z. Wang, S. Cheng, L. Li, M. Liu, H. Liu, H. Lin, Y. Zhang, *Adv. Funct. Mater.* **2020**, *31*, 2007434; h) C. Wu, F. Guo, L. Zhuang, X. Ai, F. Zhong, H. Yang, J. Qian, *ACS Energy Lett.* **2020**, *5*, 1644; i) R. Xu, X.-Q. Zhang, X.-B. Cheng, H.-J. Peng, C.-Z. Zhao, C. Yan, J.-Q. Huang, *Adv. Funct. Mater.* **2018**, *28*, 1705838; j) C. Yan, X. B. Cheng, Y. Tian, X. Chen, X. Q. Zhang, W. J. Li, J. Q. Huang, Q. Zhang, *Adv. Mater.* **2018**, *30*, 1707629.

[4] a) R. Zhang, X. B. Cheng, C. Z. Zhao, H. J. Peng, J. L. Shi, J. Q. Huang, J. Wang, F. Wei, Q. Zhang, *Adv. Mater.* **2016**, *28*, 2155; b) T. Ma, Y. Ni, Q. Wang, W. Zhang, S. Jin, S. Zheng, X. Yang, Y. Hou, Z. Tao, J. Chen, *Angew. Chem., Int. Ed. Engl.* **2022**, *61*, 202207927; c) T. Tao, S. Lu, Y. Fan, W. Lei, S. Huang, Y. Chen, *Adv. Mater.* **2017**, *29*, 1700542; d) K. Xu, M. Zhu, X. Wu, J. Liang, Y. Liu, T. Zhang, Y. Zhu, Y. Qian, *Energy Storage Mater.* **2019**, *23*, 587.

[5] a) J. Tu, W. L. Song, H. Lei, Z. Yu, L. L. Chen, M. Wang, S. Jiao, *Chem. Rev.* **2021**, *121*, 4903; b) S. Wang, S. Huang, M. Yao, Y. Zhang, Z. Niu, *Angew. Chem., Int. Ed. Engl.* **2020**, *59*, 11800; c) F. Wu, H. Yang, Y. Bai, C. Wu, *Adv. Mater.* **2019**, *31*, 1806510; d) H. Yang, H. Li, J. Li, Z. Sun, K. He, H. M. Cheng, F. Li, *Angew. Chem., Int. Ed. Engl.* **2019**, *58*, 11978; e) Z. Yuan, Q. Lin, Y. Li, W. Han, L. Wang, *Adv. Mater.* **2023**, *35*, 2211527; f) Y. Zhang, S. Liu, Y. Ji, J. Ma, H. Yu, *Adv. Mater.* **2018**, *30*, 1706310; g) P. Liu, J. Zhang, L. Zhong, S. Huang, L. Gong, D. Han, S. Wang, M. Xiao, Y. Meng, *Small* **2021**, *17*, 2102454; h) W. Liu, W. Li, D. Zhuo, G. Zheng, Z. Lu, K. Liu, Y. Cui, *ACS Cent. Sci.* **2017**, *3*, 135; i) X. Liu, J. Liu, T. Qian, H. Chen, C. Yan, *Adv. Mater.* **2019**, *32*, 1902724; j) Y. Liu, D. Lin, P. Y. Yuen, K. Liu, J. Xie, R. H. Dauskardt, Y. Cui, *Adv. Mater.* **2017**, *29*, 1605531; k) E. Faegh, B. Ng, D. Hayman, W. E. Mustain, *Nat. Energy* **2020**, *6*, 21.

[6] a) G. Cohn, L. Ma, L. A. Archer, *J. Power Sources* **2015**, *283*, 416; b) T. Gao, X. Li, X. Wang, J. Hu, F. Han, X. Fan, L. Suo, A. J. Pearse, S. B. Lee, G. W. Rubloff, K. J. Gaskell, M. Noked, C. Wang, *Angew. Chem., Int. Ed. Engl.* **2016**, *55*, 9898; c) W. Chu, X. Zhang, J. Wang, S. Zhao, S. Liu, H. Yu, *Energy Storage Mater.* **2019**, *22*, 418; d) Z. Lin, M. Mao, C. Yang, Y. Tong, Q. Li, J. Yue, G. Yang, Q. Zhang, L. Hong, X. Yu, L. Gu, Y. S. Hu, H. Li, X. Huang, L. Suo, L. Chen, *Sci. Adv.* **2021**, *7*, eabg6314; e) Y. Liu, Q. Sun, W. Li, K. R. Adair, J. Li, X. Sun, *Green Energy Environ.* **2017**, *2*, 246; f) Z. Liu, J. Wang, H. Ding, S. Chen, X. Yu, B. Lu, *ACS Nano* **2018**, *12*, 8456; g) L. Qin, D. Zhai, W. Lv, W. Yang, J. Huang, S. Yao, J. Cui, W.-G. Chong, J.-Q. Huang, F. Kang, J.-K. Kim, Q.-H. Yang, *Nano Energy* **2017**, *40*, 258; h) C. Chen, Q. Liang, Z. Chen, W. Zhu, Z. Wang, Y. Li, X. Wu, X. Xiong, *Angew. Chem., Int. Ed. Engl.* **2021**, *60*, 26718; i) S. Li, L. Fan, Y. Lu, *Energy Storage Mater.* **2019**, *18*, 205.

[7] a) Y. Zhang, L. Ma, R. Tang, X. Zheng, X. Wang, Y. Dong, G. Kong, F. Zhao, L. Wei, *Int. J. Hydrogen Energy* **2021**, *46*, 4936; b) Y. Yang, H. Yang, X. Wang, Y. Bai, C. Wu, *J. Energy Chem.* **2022**, *64*, 144; c) X. Li, Q. Guan, Z. Zhuang, Y. Zhang, Y. Lin, J. Wang, C. Shen, H. Lin, Y. Wang, L. Zhan, L. Ling, *ACS Nano* **2023**, *17*, 1653; d) G. A. Elia, K. V. Kravchyk, M. V. Kovalenko, J. Chacón, A. Holland, R. G. A. Wills, *J. Power Sources* **2021**, *481*, 228870; e) L. Wang, X. Song, Y. Hu, W. Yan, Z. Tie, Z. Jin, *Energy Storage Mater.* **2022**, *44*, 461.

[8] a) J. Ryu, M. Park, J. Cho, *Adv. Mater.* **2019**, *31*, 1804784; b) J. Wang, J. Xu, Z. Huang, G. Fan, *Fullerenes, Nanotubes Carbon Nanostruct.* **2020**, *29*, 39; c) Z. Wang, X. Zheng, A. Chen, Y. Han, L. Wei, J. Li, *ACS Mater. Lett.* **2022**, *4*, 1436; d) H. Yang, L. Yin, J. Liang, Z. Sun, Y. Wang, H. Li, K. He, L. Ma, Z. Peng, S. Qiu, C. Sun, H. M. Cheng, F. Li, *Angew. Chem., Int. Ed. Engl.* **2018**, *57*, 1898; e) X. Yu, A. Manthiram, *Adv. Funct. Mater.* **2020**, *30*, 2004084; f) D. Zhang, W. Chu, D. Y. Wang, S. Li, S. Zhao, X. Zhang, Y. Fu, H. Yu, *Adv. Funct. Mater.* **2022**, *32*, 2205562; g) D. Zhang, X. Zhang, B. Wang, S. He, S. Liu, M. Tang, H. Yu, *J. Mater. Chem. A* **2021**, *9*, 8966.

[9] a) E. Zhang, J. Wang, B. Wang, X. Yu, H. Yang, B. Lu, *Energy Storage Mater.* **2019**, *23*, 72; b) X. Zhang, Y. Tang, F. Zhang, C.-S. Lee, *Adv. Energy Mater.* **2016**, *6*, 1502588.

[10] L. Xing, K. A. Owusu, X. Liu, J. Meng, K. Wang, Q. An, L. Mai, *Nano Energy* **2021**, *79*, 105384.

[11] a) Y. Guo, Z. Hu, J. Wang, Z. Peng, J. Zhu, H. Ji, L. J. Wan, *Angew. Chem., Int. Ed. Engl.* **2020**, *59*, 22963; b) A. Bhowmik, D. Carrasco-Busturia, P. Jankowski, R. Raccichini, N. Garcia-Araez, J. M. García-Lastra, *J. Phys. Chem. C* **2022**, *126*, 40; c) W. Chu, S. He, S. Liu, X. Zhang, S. Li, H. Yu, *Chem. Commun.* **2022**, *58*, 11539.

[12] a) Y. Ai, S.-C. Wu, F. Zhang, X. Zhang, R. Li, Y. Lan, L. Cai, W. Wang, *Energy Storage Mater.* **2022**, *48*, 297; b) P. Bhauriyal, S. Das, B. Pathak, *J. Phys. Chem. C* **2020**, *124*, 11317; c) P. Bhauriyal, B. Pathak, *Mater. Adv.* **2020**, *1*, 3572; d) Z. Hu, S. Xie, Y. Guo, Y. Ye, J. Zhang, S. Jin, H. Ji, *J Energy Chem* **2022**, *67*, 354; e) H. M. Kim, J. Y. Hwang, D. Aurbach, Y. K. Sun, *J. Phys. Chem. Lett.* **2017**, *8*, 5331; f) S. Licht, *J. Electrochem. Soc.* **2019**, *144*, L133; g) S. Lysgaard, J. M. García Lastra, *J. Phys. Chem. C* **2021**, *125*, 16444; h) J. Smajic, S. Wee, F. R. F. Simoes, M. N. Hedhili, N. Wehbe, E. Abou-Hamad, P. M. F. J. Costa, *ACS Appl. Energy Mater.* **2020**, *3*, 6805.

[13] a) H. Li, J. Lampkin, N. Garcia-Araez, *ChemSusChem* **2021**, *14*, 3139; b) H. Wang, S. Gu, Y. Bai, S. Chen, N. Zhu, C. Wu, F. Wu, *J. Mater. Chem. A* **2015**, *3*, 22677; c) H. Yang, L. Yin, J. Liang, Z. Sun, Y. Wang, H. Li, K. He, L. Ma, Z. Peng, S. Qiu, C. Sun, H.-M. Cheng, F. Li, *Angew. Chem., Int. Ed.* **2018**, *57*, 1898; d) X. Yu, A. Manthiram, *Adv. Energy Mater.* **2017**, *7*, 1700561; e) L. Jia, J. Wang, S. Ren, G. Ren, X. Jin, L. Kao, X. Feng, F. Yang, Q. Wang, L. Pan, Q. Li, Y. s. Liu, Y. Wu, G. Liu, J. Feng, S. Fan, Y. Ye, J. Guo, Y. Zhang, *Energy Environ. Mater.* **2020**, *4*, 222.

[14] a) H. Chen, H. Xu, B. Zheng, S. Wang, T. Huang, F. Guo, W. Gao, C. Gao, *ACS Appl. Mater. Interfaces* **2017**, *9*, 22628; b) D. Lee, G. Lee, Y. Tak, *Nanotechnology* **2018**, *29*, 36LT01; c) H. Wang, S. Gu, Y. Bai, S. Chen, F. Wu, C. Wu, *ACS Appl. Mater. Interfaces* **2016**, *8*, 27444; d) L. Li, H. Tu, J. Wang, M. Wang, W. Li, X. Li, F. Ye, Q. Guan, F. Zhu, Y. Zhang, Y. Hu, C. Yan, H. Lin, M. Liu, *Adv. Funct. Mater.* **2023**, *33*, 2212499.

[15] a) R. Marassi, G. Mamantov, J. Q. Chambers, *J. Electrochem. Soc.* **2019**, *123*, 1128; b) R. Marassi, T. M. Laher, D. S. Trimble, G. Mamantov, *J. Electrochem. Soc.* **2019**, *132*, 1639.

[16] a) Y. Bian, Y. Li, Z. Yu, H. Chen, K. Du, C. Qiu, G. Zhang, Z. Lv, M.-C. Lin, *ChemElectroChem* **2018**, *5*, 3607; b) J. Lampkin, H. Li, L. Furness, R. Raccichini, N. Garcia-Araez, *ChemSusChem* **2020**, *13*, 3514.

[17] a) H. Li, R. Meng, Y. Guo, B. Chen, Y. Jiao, C. Ye, Y. Long, A. Tadich, Q. H. Yang, M. Jaroniec, S. Z. Qiao, *Nat. Commun.* **2021**, *12*, 5714; b) X. Yu, M. J. Boyer, G. S. Hwang, A. Manthiram, *Chem* **2018**, *4*, 586.

[18] a) Y. Guo, Z. Hu, Y. Cui, J. Wang, S. Jin, Z. Peng, H. Ji, *Batteries Supercaps* **2022**, *5*, 2100355; b) R. Jay, A. L. Jadhav, L. W. Gordon, R. J. Messinger, *Chem. Mater.* **2022**, *34*, 4486; c) Z. Du, X. Chen, W. Hu, C. Chuang, S. Xie, A. Hu, W. Yan, X. Kong, X. Wu, H. Ji, L. J. Wan, *J. Am. Chem. Soc.* **2019**, *141*, 3977; d) Y. Li, G. Chen, J. Mou, Y. Liu, S. Xue, T. Tan, W. Zhong, Q. Deng, T. Li, J. Hu, C. Yang, K. Huang, M. Liu, *Energy Storage Mater.* **2020**, *28*, 196; e) X. Meng, X. Liu, X. Fan, X. Chen, S. Chen, Y. Meng, M. Wang, J. Zhou, S. Hong, L. Zheng, G. Shi, C. W. Bielawski, J. Geng, *Adv. Sci.* **2022**, *9*, 2103773; f) S. Xie, X. Chen, C. Wang, Y. R. Lu, T. S. Chan, C. H. Chuang, J. Zhang, W. Yan, S. Jin, H. Jin, X. Wu, H. Ji, *Small* **2022**, *18*, 2200395; g) D. Zhang, S. Wang, R. Hu, J. Gu, Y. Cui, B. Li, W. Chen, C. Liu, J. Shang, S. Yang, *Adv. Funct. Mater.* **2020**, *30*, 2002471; h) S. Zhang, X. Ao, J. Huang, B. Wei, Y. Zhai, D. Zhai, W. Deng, C. Su, D. Wang, Y. Li, *Nano Lett.* **2021**, *21*, 9691.

[19] a) N. Zhu, K. Zhang, F. Wu, Y. Bai, C. Wu, *Energy Mater. Adv.* **2021**, *2021*, 9204217; b) Y. Pan, S. Li, M. Yin, J. Li, *Energy Technol.* **2019**, *7*, 1900164; c) J. Wang, L. Jia, H. Liu, C. Wang, J. Zhong, Q. Xiao, J. Yang, S. Duan, K. Feng, N. Liu, W. Duan, H. Lin, Y. Zhang, *ACS Appl. Mater. Interfaces* **2020**, *12*, 12727; d) J. Wang, S. Cheng, L. Li, L. Jia, J. Wu, X. Li, Q. Guan, H. Hu, J. Zhang, H. Lin, *Chem. Eng. J.* **2022**, *446*, 137291; e) J. Zhang, C. You, W. Zhang, J. Wang, S. Guo, R. Yang, Y. Xu, *Electrochim. Acta* **2017**, *250*, 159.

[20] a) X. Liu, Y. Li, X. Xu, L. Zhou, L. Mai, *J. Energy Chem.* **2021**, *61*, 104; b) J. Wang, S. Cheng, W. Li, S. Zhang, H. Li, Z. Zheng, F. Li, L. Shi, H. Lin, Y. Zhang, *J. Power Sources* **2016**, *321*, 193.

[21] a) M. Klimpel, M. V. Kovalenko, K. V. Kravchyk, *Commun. Chem.* **2022**, *5*, 77; b) J. Wang, S. Cheng, W. Li, L. Jia, Q. Xiao, Y. Hou, Z. Zheng, H. Li, S. Zhang, L. Zhou, M. Liu, H. Lin, Y. Zhang, *Nano Energy* **2017**, *40*, 390; c) S. Cheng, J. Wang, S. Duan, J. Zhang, Q. Wang, Y. Zhang, L. Li, H. Liu, Q. Xiao, H. Lin, *Chem. Eng. J.* **2021**, *417*, 128172.

[22] a) Q. Ran, H. Shi, H. Meng, S. P. Zeng, W. B. Wan, W. Zhang, Z. Wen, X. Y. Lang, Q. Jiang, *Nat. Commun.* **2022**, *13*, 576; b) J. Zhang, L. Jia, H. Lin, J. Wang, *Adv. Energy Sustainability Res.* **2022**, *3*, 2100187; c) J. Zhang, R. He, Q. Zhuang, X. Ma, C. You, Q. Hao, L. Li, S. Cheng, L. Lei, B. Deng, X. Li, H. Lin, J. Wang, *Adv. Sci.* **2022**, *9*, 2202244.

[23] a) Y. Bian, W. Jiang, Y. Zhang, L. Zhao, X. Wang, Z. Lv, S. Zhou, Y. Han, H. Chen, M. C. Lin, *ChemSusChem* **2022**, *15*, 202101398; b) D. Chen, S. Huang, L. Zhong, S. Wang, M. Xiao, D. Han, Y. Meng, *Adv. Funct. Mater.* **2019**, *30*, 1907717.

[24] a) T. Tsuda, J. Sasaki, Y. Uemura, T. Kojima, H. Senoh, S. Kuwabata, *Chem. Commun.* **2022**, *58*, 1518; b) X. Zheng, R. Tang, Y. Zhang, L. Ma, X. Wang, Y. Dong, G. Kong, L. Wei, *Sustainable Energy Fuels* **2020**, *4*, 1630.

[25] X. Xiao, J. Tu, Z. Huang, S. Jiao, *Phys. Chem. Chem. Phys.* **2021**, *23*, 10326.

[26] a) J. Zhang, C. You, H. Lin, J. Wang, *Energy Environ. Mater.* **2021**, *5*, 731; b) J. Cai, C. Wu, Y. Zhu, K. Zhang, P. K. Shen, *J. Power Sources* **2017**, *341*, 165; c) G. Cao, Z. Wang, D. Bi, J. Zheng, Q. Lai, Y. Liang, *Chem.- Eur. J.* **2020**, *26*, 10314; d) A. Chen, Q. Li, Z. Chen, C. Zhi, *Adv. Energy Sustainability Res.* **2021**, *2*, 2000096.

[27] J. Zhang, S. Duan, C. You, J. Wang, H. Liu, S. Guo, W. Zhang, R. Yang, *J. Mater. Chem. A* **2020**, *8*, 22240.

[28] X. Zheng, Z. Wang, J. Li, L. Wei, *Sci. China Mater.* **2022**, *65*, 1463.

[29] P. Mu, T. Dong, H. Jiang, M. Jiang, Z. Chen, H. Xu, H. Zhang, G. Cui, *Energy Fuels* **2021**, *35*, 1966.

[30] a) J. Wang, L. Jia, H. Lin, Y. Zhang, *ChemSusChem* **2020**, *13*, 3404; b) M. Zhang, W. Chen, L. Xue, Y. Jiao, T. Lei, J. Chu, J. Huang, C. Gong, C. Yan, Y. Yan, Y. Hu, X. Wang, J. Xiong, *Adv. Energy Mater.* **2019**, *10*, 1903008.

[31] Y. Guo, H. Jin, Z. Qi, Z. Hu, H. Ji, L.-J. Wan, *Adv. Funct. Mater.* **2019**, *29*, 1807676.

[32] J. Wang, L. Jia, J. Zhong, Q. Xiao, C. Wang, K. Zang, H. Liu, H. Zheng, J. Luo, J. Yang, H. Fan, W. Duan, Y. Wu, H. Lin, Y. Zhang, *Energy Storage Mater.* **2019**, *18*, 246.

[33] F. Wang, M. Jiang, T. Zhao, P. Meng, J. Ren, Z. Yang, J. Zhang, C. Fu, B. Sun, *Nano-Micro Lett.* **2022**, *14*, 169.

[34] S. Ju, J. Ye, H. Zhang, W. Wang, G. Xia, W. Cui, Y. Yang, H. Pan, X. Yu, *Energy Storage Mater.* **2023**, *56*, 1.

[35] S. Ju, C. Yuan, J. Zheng, L. Yao, T. Zhang, G. Xia, X. Yu, *Energy Storage Mater.* **2022**, *52*, 524.

[36] G. Zhou, S. Zhao, T. Wang, S. Z. Yang, B. Johannessen, H. Chen, C. Liu, Y. Ye, Y. Wu, Y. Peng, C. Liu, S. P. Jiang, Q. Zhang, Y. Cui, *Nano Lett.* **2020**, *20*, 1252.

[37] a) Z.-Q. Jin, Y.-G. Liu, W.-K. Wang, A.-B. Wang, B.-W. Hu, M. Shen, T. Gao, P.-C. Zhao, Y.-S. Yang, *Energy Storage Mater.* **2018**, *14*, 272; b) C. B. S. Sungjemmenla, V. Kumar, *Nanoscale Adv.* **2021**, *3*, 1569.

[38] W. Wang, Z. Cao, G. A. Elia, Y. Wu, W. Wahyudi, E. Abou-Hamad, A.-H. Emwas, L. Cavallo, L.-J. Li, J. Ming, *ACS Energy Lett.* **2018**, *3*, 2899.

[39] L. Ma, Y. Lv, J. Wu, Y. Chen, Z. Jin, *Adv. Energy Mater.* **2021**, *11*, 2100770.

[40] S. He, D. Zhang, X. Zhang, S. Liu, W. Chu, H. Yu, *Adv. Energy Mater.* **2021**, *11*, 2100769.

[41] K. A. Paulsen, R. A. Osteryoung, *J. Am. Chem. Soc.* **2002**, *98*, 6866.

[42] a) S. Licht, J. Hwang, T. S. Light, R. Dillon, *J. Electrochem. Soc.* **2019**, *144*, 948; b) D. Peramunage, R. Dillon, S. Licht, *J. Power Sources* **1993**, *45*, 311.

[43] Z. Hu, Y. Guo, H. Jin, H. Ji, L. J. Wan, *Chem. Commun.* **2020**, *56*, 2023.

[44] T. Gao, M. Noked, A. J. Pearse, E. Gillette, X. Fan, Y. Zhu, C. Luo, L. Suo, M. A. Schroeder, K. Xu, S. B. Lee, G. W. Rubloff, C. Wang, *J. Am. Chem. Soc.* **2015**, *137*, 12388.

[45] Y. Zhang, B. Liu, E. Hitz, W. Luo, Y. Yao, Y. Li, J. Dai, C. Chen, Y. Wang, C. Yang, H. Li, L. Hu, *Nano Res.* **2017**, *10*, 1356.

[46] a) J. Wang, H. Hu, J. Zhang, L. Li, L. Jia, Q. Guan, H. Hu, H. Liu, Y. Jia, Q. Zhuang, S. Cheng, M. Huang, H. Lin, *Energy Storage Mater.* **2022**, *52*, 210; b) J. Wang, L. Li, H. Hu, H. Hu, Q. Guan, M. Huang, L. Jia, H. Adenusi, K. V. Tian, J. Zhang, S. Passerini, H. Lin, *ACS Nano* **2022**, *16*, 17729; c) J. Wang, J. Zhang, S. Cheng, J. Yang, Y. Xi, X. Hou, Q. Xiao, H. Lin, *Nano Lett.* **2021**, *21*, 3245; d) J. Wang, J. Zhang, S. Duan, L. Jia, Q. Xiao, H. Liu, H. Hu, S. Cheng, Z. Zhang, L. Li, W. Duan, Y. Zhang, H. Lin, *Nano Lett.* **2022**, *22*, 8008; e) X. Wang, L. Yang, N. Ahmad, L. Ran, R. Shao, W. Yang, *Adv. Mater.* **2023**, *35*, 2209140; f) X. Zheng, Z. Cao, W. Luo, S. Weng, X. Zhang, D. Wang, Z. Zhu, H. Du, X. Wang, L. Qie, H. Zheng, Y. Huang, *Adv. Mater.* **2023**, *35*, 2210115; g) N. Sun, R. Li, Y. Zhao, H. Zhang, J. Chen, J. Xu, Z. Li, X. Fan, X. Yao, Z. Peng, *Adv. Energy Mater.* **2022**, *12*, 2200621.

[47] a) X. Liang, Q. Pang, I. R. Kochetkov, M. S. Sempere, H. Huang, X. Sun, L. F. Nazar, *Nat. Energy* **2017**, *2*, 17119; b) Z. Tu, S. Choudhury, M. J. Zachman, S. Wei, K. Zhang, L. F. Kourkoutis, L. A. Archer, *Nat. Energy* **2018**, *3*, 310.

[48] a) D. He, W. Cui, X. Liao, X. Xie, M. Mao, X. Sang, P. Zhai, Y. Zhao, Y. Huang, W. Zhao, *Adv. Sci.* **2022**, *9*, 2105656; b) J. Wan, W. Chen, C. Jia, L. Zheng, J. Dong, X. Zheng, Y. Wang, W. Yan, C. Chen, Q. Peng, D. Wang, Y. Li, *Adv. Mater.* **2018**, *30*, 1705369; c) H. Wang, H. Cheng, D. Li, F. Li, Y. Wei, K. Huang, B. Jiang, H. Xu, Y. Huang, *Adv. Energy Mater.* **2023**, *13*, 2204425.

[49] a) X. Zhang, X. Li, Y. Zhang, X. Li, Q. Guan, J. Wang, Z. Zhuang, Q. Zhuang, X. Cheng, H. Liu, J. Zhang, C. Shen, H. Lin, Y. Wang, L. Zhan, L. Ling, *Adv. Funct. Mater.* **2023**, 2302624. https://doi.org/10.1002/adfm.202302624; b) J. Wang, J. Zhang, J. Wu, M. Huang, L. Jia, L. Li, Y. Zhang, H. Hu, F. Liu, Q. Guan, M. Liu, H. Adenusi, H. Lin, S. Passerini, *Adv. Mater.* **2023**, 2302828. https://doi.org/10.1002/adma.202302828.

Jing Zhang is a assistant reseacher at School of Materials Science and Engineering at Xi'an University of Technology, Xi'an, China. She received her Ph.D. degree in materials physics and chemistry at Xi'an University of Technology in 2020. Her researches currently focus on functional catalysis materials synthesis and interface characterization in Metal–S batteries.

Caiyin You is now a professor at School of Materials Science & Engineering at Xi'an University of Technology, Xi'an, China. After receiving his Ph.D. degree in 2003 from Institute of Metal Research, Chinese Academy of Sciences, he used to work in National Institute for Material Science, Japan and University of Oxford, UK, from 2003 to 2009. His current research interests mainly focus on magnetic materials and energy-related materials.

Hongzhen Lin is a senior researcher at *i*-lab of Suzhou Institute of Nano-Tech and Nano-Bionics, Chinese Academy of Sciences and University of Science and Technology of China. He majors in developing high energy density lithium metal-based energy storage systems with catalytic functionalities and their in situ interfacial nonlinear spectroscopy characterization.

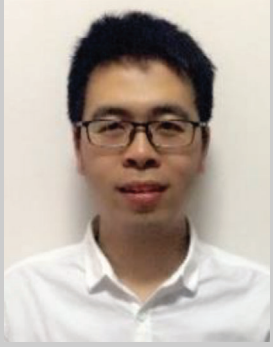

Jian Wang is currently a research fellow supported by Alexander von Humboldt foundation in Helmholtz Institute Ulm after receiving his Ph.D. degree from University of Science and Technology of China. His research interests focus on the applications of highly active catalysts in secondary batteries (Catalysis-in-Batteries) and the exploration of in situ characterizations for probing catalytic mechanisms.